AGU PUBLICATIONS

JGR

Journal of Geophysical Research: Oceans

RESEARCH ARTICLE

10.1002/2017JC012698

**Key Points:**
- Two years of new observations of ISOW transport through the CGFZ yield a mean value of −1.7 Sv, 30% lower than the previous direct measurement
- The previous mean ISOW transport estimate may have been biased high by the use of a single realization of ISOW layer thickness that was 33% larger than the new 2 year mean
- Most of the observed ISOW transport variability is tightly linked to the presence or absence of the NAC in the CGFZ

**Supporting Information:**
- Supporting Information S1

**Correspondence to:**
A. Bower,
abower@whoi.edu

**Citation:**
Bower, A. and H. Furey (2017), Iceland-Scotland Overflow Water transport variability through the Charlie-Gibbs Fracture Zone and the impact of the North Atlantic Current, *J. Geophys. Res. Oceans*, *122*, 6989–7012, doi:10.1002/2017JC012698.

Received 12 JAN 2017
Accepted 21 JUL 2017
Accepted article online 5 AUG 2017
Published online 1 SEP 2017



# Iceland-Scotland Overflow Water transport variability through the Charlie-Gibbs Fracture Zone and the impact of the North Atlantic Current

**Amy Bower[1] and Heather Furey[1]**

[1]Woods Hole Oceanographic Institution, Woods Hole, Massachusetts, USA

**Abstract** The Charlie-Gibbs Fracture Zone (CGFZ), a deep and wide gap in the Mid-Atlantic Ridge near 52°N, is a gateway between the eastern and western subpolar regions for the Atlantic Meridional Overturning Circulation (AMOC). In 2010–2012, an eight-mooring array of current meters and temperature/salinity sensors was installed across the CGFZ between 500 m and the sea floor to measure the mean transport of westward-flowing Iceland-Scotland Overflow Water (ISOW) and investigate the impact of the eastward-flowing North Atlantic Current (NAC) on ISOW transport variability. The 22 month record mean ISOW transport through the CGFZ, $-1.7 \pm 0.5$ Sv (95% confidence interval), is 30% lower than the previously published estimate based on 13 months of current-only measurements, $-2.4 \pm 1.2$ Sv. The latter mean estimate may have been biased high due to the lack of continuous salinity measurements, although the two estimates are not statistically different due to strong mesoscale variability in both data sets. Empirical Orthogonal Function analysis and maps of satellite-derived absolute dynamic topography show that weak westward ISOW transport events and eastward reversals are caused by northward meanders of the NAC, with its deep-reaching eastward velocities. These results add to growing evidence that a significant fraction of ISOW exits the Iceland Basin by routes other than the CGFZ.

## 1. Introduction

The oceanic Meridional Overturning Circulation (MOC) is a global system of deep and shallow currents that redistributes heat, freshwater, carbon, and other properties over the largest spatial scales, and thus it is a vital component of Earth's climate system. The Atlantic MOC (AMOC) is considered to be the strongest part of the global MOC [*Trenberth and Caron*, 2001] and, in the North Atlantic, contributes ∼25% of the total (ocean plus atmosphere) poleward heat flux [*Srokosz and Bryden*, 2015, and references therein; *Lozier et al*., 2017].

While considerable observational effort has been made to describe the structure of primary AMOC currents—and in some cases, their low-frequency variability—at a selected number of locations [e.g., *Rossby et al*., 2010; *Willis*, 2010; *Meinen et al*., 2010; *Toole et al*., 2011; *Send et al*., 2011; *Smeed et al*., 2014; *Roessler et al*., 2015; *Mercier et al*., 2015; *Daniault et al*., 2016; *Lozier et al*., 2017], little attention has been paid over the past nearly three decades to the Charlie-Gibbs Fracture Zone (CGFZ), where branches of both the warm and cold limbs of the AMOC cross the Mid-Atlantic Ridge (MAR; Figure 1). At depth, dense Iceland-Scotland Overflow Water (ISOW) streams westward through the deep CGFZ into the western North Atlantic, where it eventually joins the other components of North Atlantic Deep Water (NADW) in the Deep Western Boundary Current (DWBC) [see *McCartney*, 1992, *Dickson and Brown*, 1994, *Daniault et al*., 2016, for reviews]. Also in the CGFZ region, warm subtropical water, recirculating Subpolar Mode Water (SPMW), and recently convected Labrador Sea Water (LSW) are carried eastward over the MAR by the multibranched North Atlantic Current (NAC), also sometimes referred to as the Subpolar or Subarctic Front [e.g., *Sy et al*., 1992; *Belkin and Levitus*, 1996; *Rhein et al*., 2002; *Bower and von Appen*, 2008; *Roessler et al*., 2015].

The ISOW flowing westward in the CGFZ has its origins in the overflow of cold, dense Norwegian Sea water through several deep channels in the Iceland-Scotland Ridge (Figure 1) [see *Østerhus et al*., 2008, for a review]. The total overflow transport has been estimated to be about 3 Sv based on multiyear direct measurements, with the largest contribution coming from the Faroe Bank Channel and the greatest uncertainty associated with the flows over the Iceland Faroes Ridge. The main plume of the ISOW descends into the

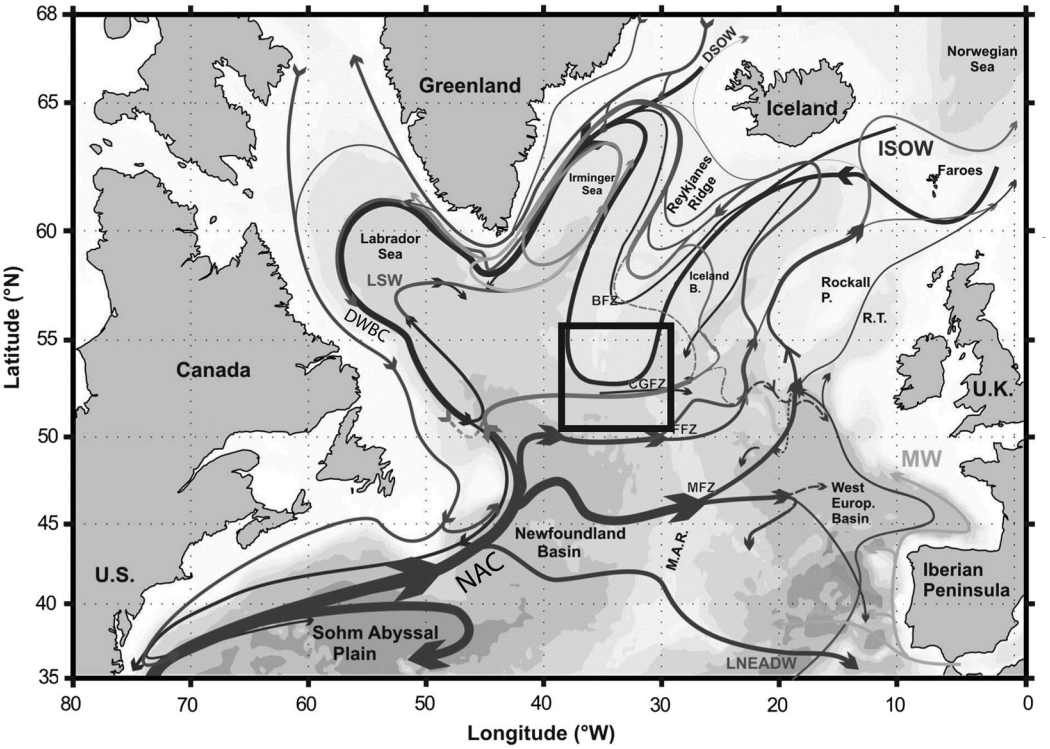


**Figure 1.** Schematic circulation diagram showing primary deep and shallow currents in the subpolar North Atlantic based on *Daniault et al.* [2016]. Bathymetry detail in the boxed area is illustrated in Figure 2a. Abbreviations include Iceland-Scotland and Denmark Strait Overflow Waters (ISOW, DSOW); Mediterranean Water (MW); Lower Northeast Atlantic Deep Water (LNEADW), also known as Lower Deep Water; Labrador Sea Water (LSW); North Atlantic Current (NAC); Deep Western Boundary Current (DWBC); Bigth Fracture Zone (BFZ); Charlie-Gibbs Fracture Zone (CGFZ), Faraday Fracture Zone (FFZ); Maxwell Fracture Zone (MFZ); Mid-Atlantic Ridge (M.A.R.); Rockall Plateau (Rockall P.); Rockall Trough (R.T.).

Iceland Basin, entraining warmer, saltier SPMW, resulting in an increase in temperature and salinity of the ISOW plume [*Mauritzen et al.*, 2005; *Fer et al.*, 2010; *Yashayaev and Dickson*, 2008, and references therein]. This is what gives ISOW its characteristic high salinity compared to the other water masses that make up NADW, namely LSW and Denmark Strait Overflow Water (DSOW).

The diluted ISOW flows southwestward along the Reykjanes Ridge as a deep boundary current in the water depth range 1600–2800 m. Several direct and indirect transport estimates have been made along this stretch of the ISOW's path, the most recent of which is $3.8 \pm 0.6$ (standard error) Sv from 2 years of current measurements near 61°N, 22°W [see *Kanzow and Zenk*, 2014, and references therein].

South of 61°N, the ISOW plume crosses over to the western basin through deep gaps in the MAR. This has historically been thought to occur primarily at the CGFZ, the widest (~100 km) and deepest (3600–3800 m) gap in the ridge north of the equator. Hydrographic studies suggest that the westward transport through this gap consists of about 50% pure ISOW, with the rest composed mainly of entrained SPMW, LSW, and remnant AABW (Antarctic Bottom Water, also called Lower Deep Water, LDW, at these latitudes) in varying proportions depending on the study [*Smethie et al.*, 2000]. The product that emerges into the western North Atlantic is sometimes referred to as Northeast Atlantic Deep Water or Gibbs Fracture Zone Water—we will continue to call it ISOW in recognition of its largest constituent water mass.

Early attempts to quantify the westward transport of deep waters through the CGFZ were made using hydrographic observations and an assumed level of no motion or a small number of subsurface floats, and range from $-4.6$ to $-6.0$ Sv [*Worthington and Volkmann*, 1965; *Harvey and Theodorou*, 1986; *McCartney*, 1992; *Schmitz and McCartney*, 1993]. All of these estimates are 2–2.5 times larger than the one direct estimate of $-2.4 \pm 0.6$ Sv (standard error) made by *Saunders* [1994] (hereafter S94) in the late 1980s. In this important first (and only) attempt to measure a longer-term mean transport of overflow waters through the CGFZ, eight current meter moorings were deployed along 35°W in the deep CGFZ for 13 months in 1988–1989 (Figures 2a

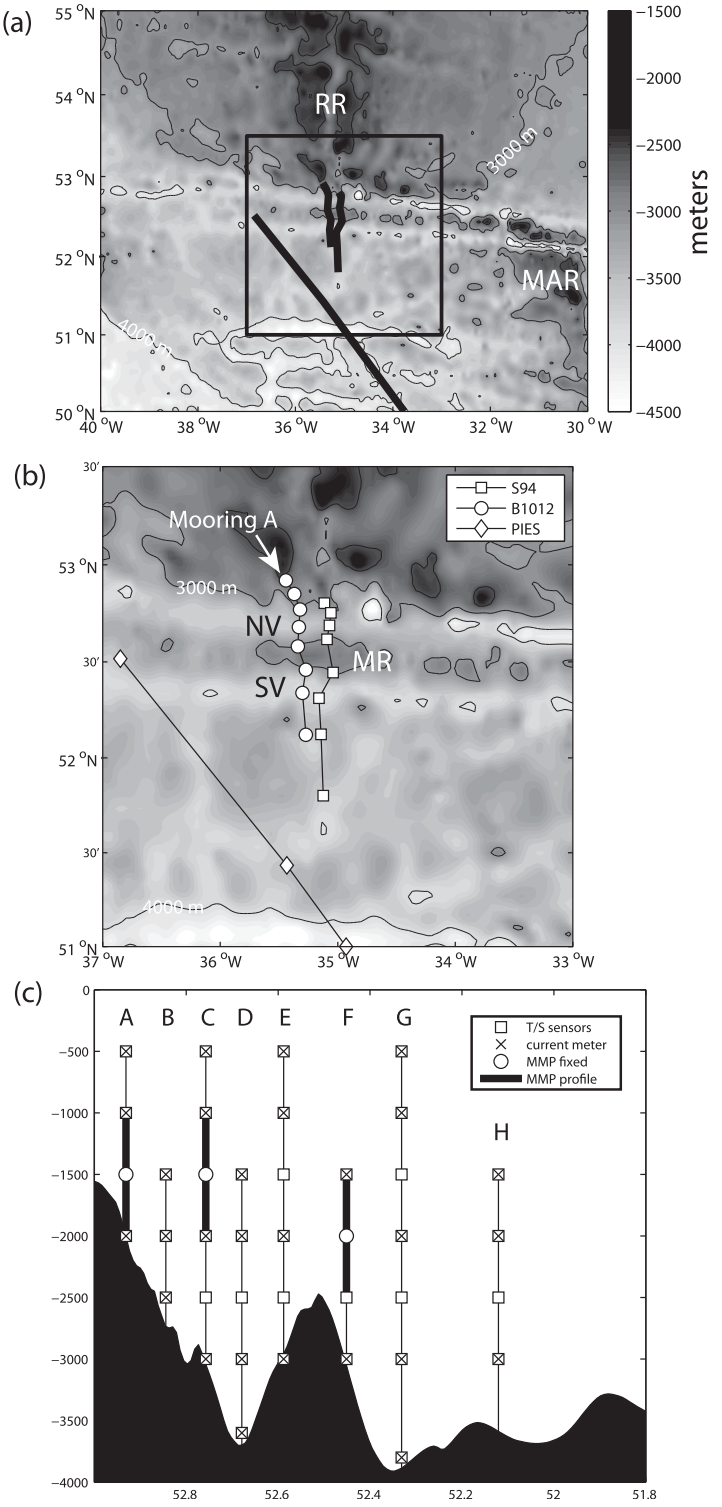


**Figure 2.** (a) Bathymetry of the CGFZ region from ETOPO2 with the Saunders (S94), Bower (B1012), and PIES (Pressure Inverted Echo Sounders) mooring lines shown. Mooring array and bathymetry details in the boxed area are shown in (b). Abbreviations include Reykjanes Ridge (RR) and Mid-Atlantic Ridge (MAR). Bathymetry is shaded, and the 3000 and 4000 m isobaths are drawn as thin black lines. (b) Bathymetry, depicted as in Figure 2a, of the CGFZ with mooring positions indicated by symbols. Locations of median ridge (MR), northern valley (NV), and southern valley (SV) are indicated. (c) Cross section of B1012 array configuration. MMP refers to McLane Moored Profiler.

and 2b). S94's mean ISOW transport estimate has been used in many reviews of ISOW and NADW circulation [e.g., *Dickson and Brown*, 1994; *Schmitz and McCartney*, 1993; *Kanzow and Zenk*, 2014; *Daniault et al*., 2016].

One of the most remarkable features of S94's ISOW transport time series is the strong variability on time scales from 10 to 400 days, with transport ranging from −10 Sv (westward) to +5 Sv (eastward). The standard deviation around the mean of −2.4 Sv westward was 3.0 Sv. S94 speculated that local interactions between the NAC and the ISOW were largely responsible for this variability, but he did not have the observations to confirm this hypothesis.

Some support for S94's hypothesis was provided by *Schott et al*. [1999], who collected a top-to-bottom synoptic section of absolute velocity across the CGFZ at 35°W with Lowered Acoustic Doppler Current Profiler (LADCP) in August 1997. They observed that eastward currents occupied the entire CGFZ, and the transport below 1500 m was 6.5 Sv eastward. Like S94, *Schott et al*. [1999] surmised that a northward meander or eddy of the NAC was disrupting the westward transport of overflow water, based on a regional vessel-mounted ADCP survey. *Bower and von Appen* [2008] confirmed with satellite altimetry that a branch of the NAC with surface geostrophic velocities as high as 12 cm/s was flowing eastward through the CGFZ across 35°W at the time of Schott's LADCP observations. A deep extension of this current branch could explain the deep eastward velocities and apparent blocking of the westward ISOW transport through the CGFZ.

The frequency and duration of such northward extensions of

the NAC have historically been difficult to determine from occasional hydrographic measurements due to multiple current branches, large-amplitude, time-dependent meanders and cut-off eddies. Infrared imagery is of almost no use due to persistent cloudiness in this region. Several hydrographic studies have indicated that the northern branch of the NAC appears to be quasi-locked over the CGFZ, possibly because this southern boundary of the subpolar gyre is more barotropic and therefore more constrained by bathymetry than the other NAC branches [*Meincke and Sy*, 1983; *Sy*, 1988; *Sy et al*., 1992; *Belkin and Levitus*, 1996]. *Bower et al*. [2002] and *Bower and von Appen* [2008] found that acoustically tracked floats drifting eastward in the NAC at the thermocline level (i.e., well above the ridge crest) preferentially crossed over the ridge at the latitudes of the CGFZ and the next fracture zone to the south, the Faraday Fracture Zone (FFZ; 50–51°N), suggesting that indeed there is a tendency for the NAC to be funneled through, or over, gaps in the MAR.

Here we report on observations from a new eight-mooring array deployed for nearly 2 years (2010–2012) in the CGFZ with the objectives of improving the estimate of mean ISOW transport through the CGFZ and investigating in detail the interaction between ISOW transport and the NAC. The new array, here referred to as B1012, measured currents, temperature, and salinity in the CGFZ over most of the water column, providing complete coverage of the ISOW layer, simultaneous measurements of deep and upper ocean currents, and continuous salinity observations. Furthermore, gridded sea surface height maps, not available at the time of S94's moored measurements, provide the larger spatial and temporal context for interpreting the B1012 measurements. These and other ancillary data sets are described in the next section. In section 3, we first compare the B1012 array mean currents and salinity in the CGFZ with S94. We then present the new estimate of mean ISOW transport and discuss the implications of methodological differences on the B1012 and S94 transport calculations. Following this, we use in situ current observations and altimeter-derived sea surface height to document and quantify the impact of the NAC on ISOW transport. The results are discussed and summarized in section 4.

## 2. Data and Methods

### 2.1. Mooring Arrays

The B1012 mooring array was set during 18–21 August 2010 from the German Meteor cruise M-82/2 (M. Rhein, chief scientist) and recovered during 28–30 June 2012 from the German Maria S. Merian cruise MSM-21/2 (D. Kieke, chief scientist). Details of the cruise operations can be found in *Rhein* [2010] and *Kieke et al*. [2014]. Related cruise operations in the vicinity of the CGFZ included servicing of four Pressure Inverted Echo Sounders (PIES; Figures 2a and 2b) aimed at a complementary investigation of NAC transport and pathway variability in the vicinity of the MAR since 2006 [*Rhein et al*., 2011; *Roessler et al*., 2015].

The B1012 array was in full operation for 677 days and consisted of eight moorings nominally along 35.33°W between 52.925°N and 52.118°N (Figures 2a and 2b, *Bower et al*., 2017). Five of the moorings (A–E) were deployed in the northern valley (NV) of the CGFZ, and three (F–G) were deployed in the southern valley (SV) and plain (H). There were four "tall" moorings extending from the sea floor to 500 m (A, C, E, and G) and four shorter moorings extending from the seafloor to 1500 m (B, D, F, and H) (Figure 2c). Table 1 summarizes the mooring positions and configurations whereas complete details can be found in *Furey et al*. [2014].

A total of 36 SBE-37 microcats sampled temperature and conductivity (and some pressure) every 15 min. Conductivity was calibrated with postcruise factory calibration coefficients. The results were within the range of bottle-corrected CTD conductivity from the deployment and recovery cruises so no further corrections were made [see *Furey et al*., 2014, for details]. Data return was 100% from the microcats except for the bottom instrument at mooring B, which returned only 50%, and the top instrument on mooring G, which returned 91%. These time series were filtered (backward and forward to eliminate phase shifts) with a low-pass second-order Butterworth filter with a 40 h cut-off period. Maximum mooring tow-down was ∼25 m at mooring C. Other moorings were pulled down less than 10 m. Therefore, no corrections were made for mooring motion.

A total of 28 current meters were arranged across the eight moorings, including 18 Aanderaa RCM-11 and 10 Nortek AquaDopp 6000 DW instruments. Velocity components were recorded every 30 min. Data return was 100% except that the 2000 m instrument on mooring G returned only 56% velocity data. The same low-pass filtering was applied as for the microcats. In addition to the current meters and microcats, three

**Table 1.** Mooring Positions and Instrument Configurations for the B1012 Array[a]

| Mooring | Position | Water Depth (m) | Mean Depth (m) | Instruments |
|---|---|---|---|---|
| A | 52.9250°N, 35.4447°W | 2000 | 476 | AM |
| | | | 976 | AM |
| | | | 1940 | NM |
| B | 52.8467°N, 35.3733°W | 2775 | 1483 | AM |
| | | | 1981 | NM |
| | | | 2713 | AM[b] |
| C | 52.7747°N, 35.324°W | 3000 | 480 | AM |
| | | | 980 | NM |
| | | | 1982 | AM |
| | | | 2482 | M |
| | | | 2944 | AM |
| D | 52.6803°N, 35.3308°W | 3725 | 1505 | AM |
| | | | 1999 | NM |
| | | | 2503 | M |
| | | | 3007 | AM |
| | | | 3687 | AM |
| E | 52.5848°N, 35.3438°W | 2975 | 523 | AM |
| | | | 1024 | NM |
| | | | 1525 | M |
| | | | 2026 | NM |
| | | | 2527 | M |
| | | | 2962 | AM |
| F | 52.459°N, 35.268°W | 3009 | 1497 | AM |
| | | | 2502 | M |
| | | | 2962 | AM |
| G | 52.3353°N, 35.2968°W | 3879 | 504 | AM[c] |
| | | | 1000 | NM |
| | | | 1500 | M |
| | | | 2001 | NM[d] |
| | | | 2502 | M |
| | | | 3005 | AM |
| | | | 3844 | AM |
| H | 52.1182°N, 35.2725°W | 3866 | 1494 | AM |
| | | | 1993 | NM |
| | | | 2495 | M |
| | | | 3167 | AM |

[a]Under instruments, M refers to Microcat, A to Aanderaa current meter, and N to Nortek current meter.
[b]Forty-eight percent data return.
[c]Ninety-one percent data return.
[d]Fifty-six percent data return.

McLane Moored Profilers (MMPs) were installed on three moorings (Figure 2c). MMP data return was mixed, and they are not considered further in this paper.

For comparison, S94 installed eight moorings along 35°W, or about 22 km east of the B1012 array (Figures 2a and 2b), from RRS Discovery cruise 174 in June 1988, and recovered them from RRS Charles Darwin cruise 42 in September 1989, for a 400 day deployment. His shallowest mooring was on the ~2500 m isobath, 500 m downslope from our shallowest mooring (Figure 2b). S94 had a total of 16 temperature-equipped Aanderaa current meters. Current meters were placed nominally at 2500 and 3000 m, as well as near the bottom in the two transform valleys of the CGFZ.

### 2.2. ISOW Transport Calculation

#### 2.2.1. *Saunders* [1994]

We estimated ISOW transport from the B1012 measurements largely following S94's method. He defined ISOW in the CGFZ as all water with salinity greater than 34.94. This was based on comparisons with previous studies, including his and earlier observations showing a correspondence between the 34.94 isohaline and the potential density 27.8 kg/m$^3$, which has historically been used to separate deep and intermediate waters in the subpolar North Atlantic [e.g., *Dickson and Brown*, 1994]. Furthermore, S94 observed a transition between clear and turbid water around the isohaline 34.94 in light attenuation profiles obtained at the time of array deployment, presumably cause by ISOW picking up sediment as it flows along the bottom.

We have used the same ISOW salinity definition here, even though decadal changes in ISOW salinity have been documented [e.g., *Sarafanov et al.*, 2007]. Layer-averaged ISOW salinity in the Iceland Basin at 60°N freshened from the 1960s until about 1997, after which its salinity increased rapidly up to at least 2007 [*Sarafanov et al.*, 2009, their Figure 7e]. As a result of these changes, salinity in 2007 was about 0.005 higher than in 1988. How much it has changed since 2007 is not reported in the literature, but a 0.005 difference in the definition of ISOW will not significantly change the transport estimates. Furthermore, the relationship between the depth of the 27.8 $\sigma\theta$ and 34.94 isohaline in 1988 (S94, his Figure 2) is very similar to that in 2010 and 2012 (Figure 3).

Since S94's shallowest current meters (2500 m) were deeper than the depth of the top interface of ISOW (which is typically 1500–2500 m), he utilized the approximate linear relationship observed between zonal speed at 3000 and 2500 m at each mooring, and assuming constant shear up to 2000 m depth, used the linear relationship to extrapolate and generate a synthetic zonal speed time series at 2000 m for each mooring. To estimate ISOW transport, S94 multiplied zonal speed by the thickness of the ISOW layer (waters with salinity greater than 34.94). With no continuous conductivity sensors in the array, S94 was forced to use a single CTD survey conducted at the time of mooring deployment to define the ISOW layer thickness. The implications of this will be discussed below.

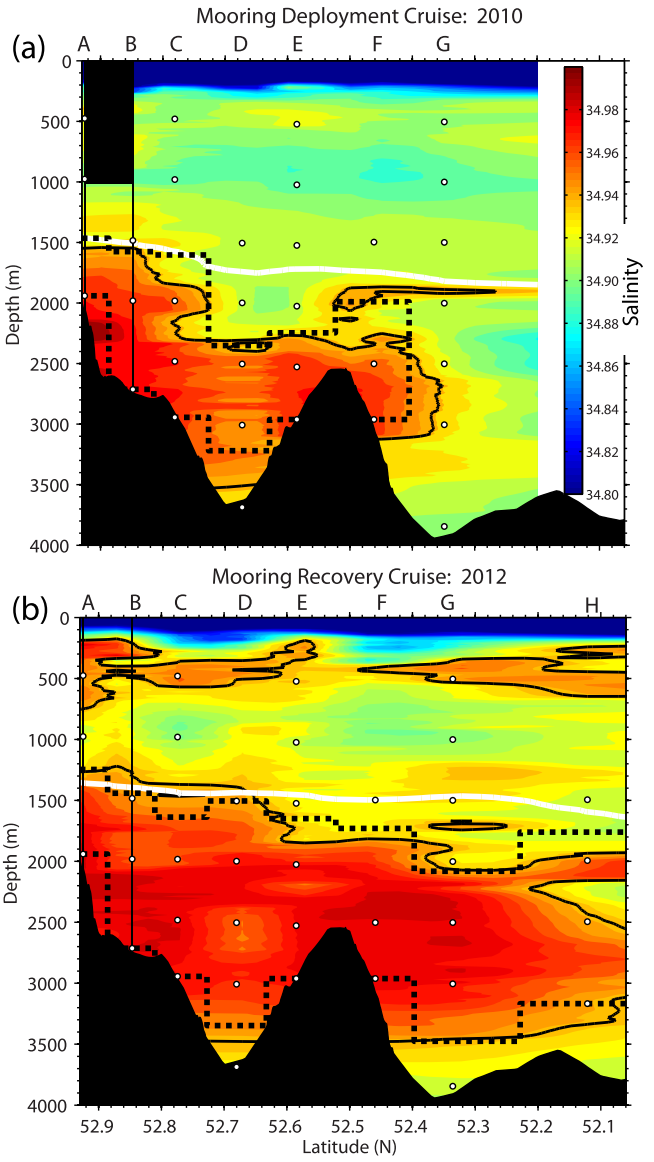


**Figure 3.** (a) Salinity section across the B1012 array from CTD profiles made at each mooring site (except H) at the time of array deployment in August 2010. Vertical black lines indicate CTD profile and mooring locations, with white circles indicating temperature/salinity sensors on the moorings. Solid black contour indicates the 34.94 isohaline, used here to define the boundaries of ISOW. Thick dashed lines show the equivalent as determined from the fixed sensors (see text for details). The $\sigma\theta = 27.8$ kg/m$^3$ contour (from CTD observations) is indicated by the white line. Water denser than this value was used by S94 as an alternative definition of the top of the ISOW layer in the CGFZ. (b) Same as Figure 3a but from CTD profiles at all mooring sites at the time of array recovery in June 2012.

#### 2.2.2. B1012 Array

To obtain the most accurate estimate possible of ISOW transport through the CGFZ, the B1012 array was configured as follows:

1. The B1012 array was sited slightly west of the S94 array to capture all streams of ISOW coming through the northern CGFZ. At the S94 site, digital bathymetric maps (not available in the 1980s) show a deep channel north of the shoal just north of S94's northernmost mooring (~53°N, see small closed 3000 m contour that marks the deepest part of this channel in Figure 2b).
2. Instruments in the B1012 array were extended shallower in the water column to assure full coverage of the ISOW layer and simultaneous measurements of ISOW and the NAC (Figure 2c).
3. One mooring (A) was placed higher up on the slope of the Reykjanes Ridge, at the 2000 m isobath, to more fully capture the less dense ISOW flowing along the midslope (Figures 2b and 2c).
4. Continuous salinity measurements were added to enable observation of time dependence in the thickness of the ISOW layer.

The steps followed to construct a time series of ISOW transport (defined as water with salinity greater than 34.94) through the B1012 array were as follows:

1. Time series of temperature, salinity, zonal, and meridional velocity at each depth were combined into daily averages.
2. Zonal speed and salinity time series were linearly interpolated vertically between sensors onto a 1 m depth vector.
3. A time series of the depth of the 34.94 isohaline was determined for each mooring site. At northern moorings, where ISOW is trapped against the bottom, there was only one such level for each time step, defined here as the top of the ISOW layer. At more southern mooring sites there was (at least) one other depth where salinity equaled 34.94, marking the lower interface of ISOW where it is found above the less saline LDW. If more than two depths were found with salinity equal to 34.94, the shallowest and deepest depths were chosen to define the top and bottom of the ISOW interface.
4. With the top and bottom of the ISOW layer defined at each time step for each mooring, zonal ISOW transport per unit distance was computed by multiplying daily ISOW thickness by the daily layer-averaged zonal speed.

5. The ISOW transport at each mooring was finally estimated by multiplying the transport per unit distance times the distance between the midpoints to each of its two flanking moorings. For the endpoint moorings (A and H), the ISOW transport per unit width was multiplied by twice the distance between mooring A(H) and the midpoint of adjacent mooring B(G). The overall transport estimate is for a cross sectional area that extends a few kilometers north and south of the array (same as S94).
6. Missing data: When data from the 2000 m current meter on G was missing, u at that depth was interpolated using the 1500 and 3000 m current meter time series. When the salinity from the bottom instrument at mooring B was missing, it was assumed that it was greater than 34.94—salinity never dropped below that level when data were available, nor did it drop below that value at the bottom of the neighboring moorings (A and C). In other words, ISOW was assumed to extend to the sea floor at mooring B for the entire record.
7. At moorings B and D, salinity at the 1500 m (top) microcat was greater than 34.94 for 27% and 12% of the time, respectively, indicating that the top interface of the ISOW layer was at times shallower than the mooring sensors. For these time steps, the depth of the 34.94 isohaline was taken to be the average of this isohaline depth at the neighboring (tall) moorings for the same time step. Sometimes that average was below 1500 m, in which case the isohaline depth at the short mooring was set to 1500 m.
8. It was also necessary to generate synthetic velocity time series up to 1000 m depth at moorings B and D to estimate transport when the top ISOW interface was above those moorings. An Empirical Orthogonal Function (EOF) analysis of zonal velocity showed that about 68% or more of the variance was associated with a vertical mode with very little shear near 1000 m depth (see more details below). Therefore, the zonal speed at 1000 m depth at moorings B and D was constructed by adding the speed fluctuations from the 1500 m instrument to the average of the time mean zonal speed from the 1000 m instruments on the two neighboring moorings.

Figure 3 compares the layer interfaces determined by linear interpolation between fixed instruments with the more accurate method using the continuous salinity profiles collected during the mooring deployment and recovery cruises. There does not seem to be any systematic bias in the approximation of the interface depths from the mooring sensors: at some sites, the sensor-based thickness overestimates the actual thickness, and at other sites, vice versa. For the deployment cruise, the sum of ISOW layer thickness across all moorings from fixed sensors was 5509 m, and from continuous profiles 5426 m (moorings A–F only; sensors would not detect the thin ISOW layer observed in the continuous profile at mooring G, and there was no CTD profile at mooring H during the deployment cruise). The mean thickness difference for moorings A–F was $20 \pm 185$ m (standard deviation), which is only 3% of the mean (by mooring) layer thickness from the continuous profiles of 775 m. During the recovery cruise, the thickness sum was 10,461 m from fixed sensors and 10,722 m from continuous profiles. Mean difference was $33 \pm 233$ m, or 2% of the thickness mean of 1340 m. These two salinity sections also illustrate the extreme temporal variability in the thickness of the ISOW layer, and portend the possible difficulty of using a time-invariant layer thickness in the transport calculation, as was done by S94 and will be discussed more below.

## 3. Results

### 3.1. Mean Velocity and Salinity Structure in the CGFZ

Figures 4a and 4b compare the structure of mean zonal currents observed by S94 and B1012. The difference in sampling is immediately obvious, but several similarities are evident in the current structure below 2500 m: (i) there are streams of relatively strong mean westward flow centered at about 2000–3000 m, banked up against the slope of the Reykjanes Ridge in the NV, and banked up against the southern slope of the median ridge in the SV; (ii) strongest mean zonal speeds are westward ($-6$ to $-8$ cm/s) at bottom instruments in both arrays (at moorings SA, SB, and SE in S94 and moorings A, C, and F in B1012—not at mooring B, possibly because it was located on a relatively flat part of the slope); and (iii) mean eastward flow was found in the bottom of both valleys in both time periods, and in the NV this eastward vein may be banked up against the northern slope of the median ridge.

Different between the two time periods is the larger width of the westward stream in the NV in S94. Mean westward currents were observed across nearly the entire channel in S94, from moorings SA through SC. In

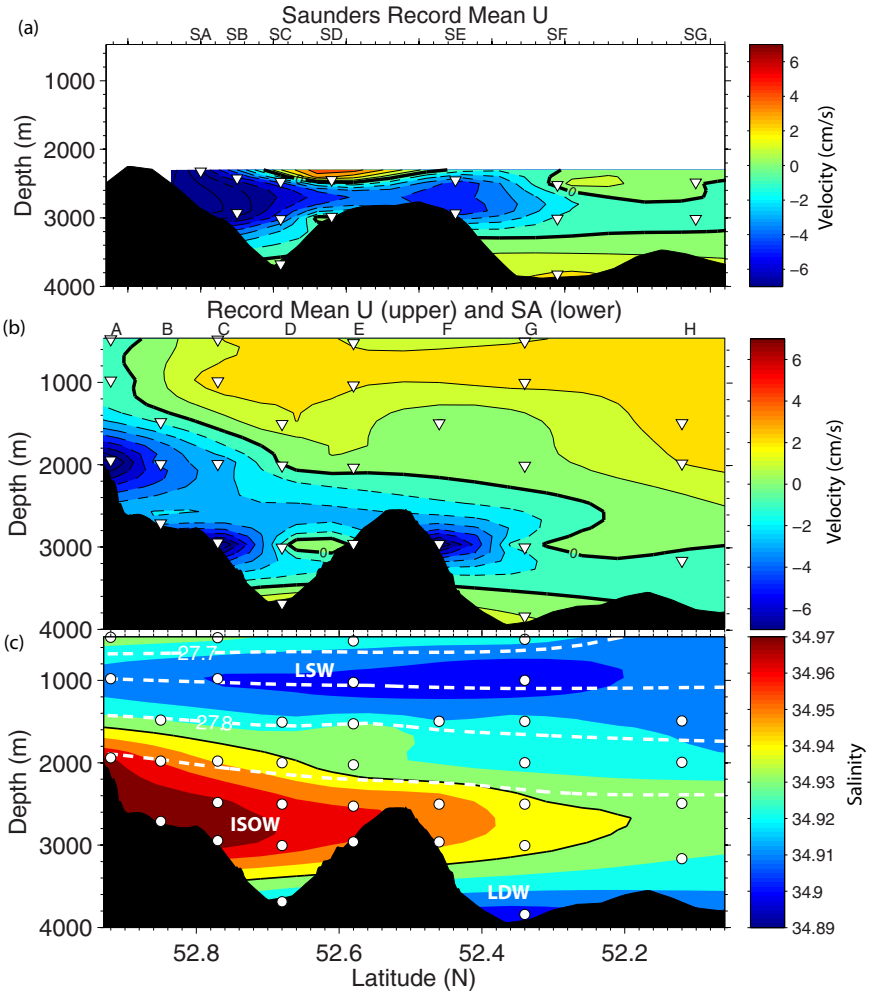


**Figure 4.** (a) Mean zonal speed in the CGFZ during 1988–1989 reproduced from statistics reported by S94 in his Table 3. Positive speeds are eastward and the thick black contour highlights the zero isotach. Moorings are labeled SA-SG (S for Saunders) and inverted triangles show current meter locations. Bathymetric profile is constructed from the ETOPO2 digital data base along the S94 mooring line (Figure 2b) to match the more northerly extent of the B1012 sections shown in (b, c) (there are some small discrepancies between ETOPO2 and water depths reported by S94, e.g., at mooring SC). Also, this section has been cut off between moorings SG and SH to match the southern limit of the B1012 array. (b) Same as Figure 4a but for the record mean zonal speeds observed during 2010–2012 by B1012. Mooring labels are shown along top axis and current meters are indicated by inverted triangles. (c) Same as Figure 4b but for mean salinity from B1012. The black contour highlights the 34.94 isohaline. White dashed lines indicate selected isopycnals, which are contoured every 0.05 kg/m$^3$. Microcats are indicated by circles. On this and subsequent cross sections, use caution when interpreting contouring between instruments, including the occasional spurious maximum or minimum between data points. Mean and standard deviations from instrumental records can be found in supporting information Table S1.

contrast, the B1012 mean velocity section shows that the mean velocity was westward at moorings A–C, and was near zero through the water column at mooring D (the equivalent mooring to mooring SC in S94).

With an additional mooring up the slope of the Reykjanes Ridge, the B1012 array shows the westward stream in the NV extending to at least the 2000 m isobath in the mean. Also evident from B1012 measurements shallower than the S94 measurements was mean eastward flow in the upper part of the array. The 1000 m instruments at moorings C, E, and G measured mean eastward speeds of 2.7, 2.1, and 2.2 cm/s, respectively (mean and standard deviation for all variables are provided in supporting information Table S1). Interestingly, weaker mean eastward currents were observed at 500 m at these moorings, namely 1.9, 1.9, and 2.0 cm/s, respectively, indicating oppositely signed vertical shear above and below these 1000 m instruments.

The mean salinity structure in the CGFZ from the B1012 microcat sensors (Figure 4c) reveals the characteristic high-salinity layer associated with ISOW, flanked above and below by fresher waters, LSW and LDW.

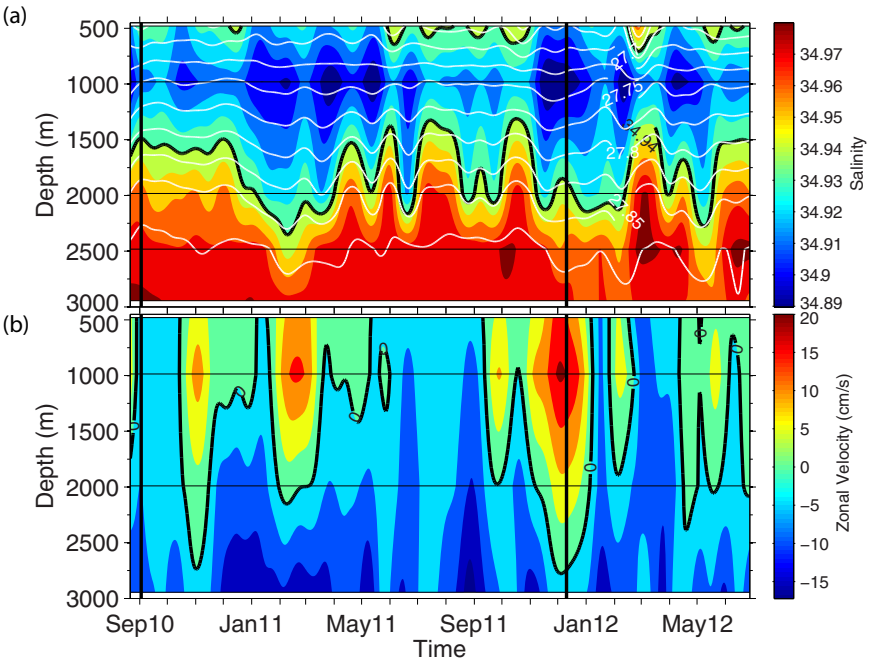


**Figure 5.** (a) Time-depth plot of salinity at mooring C after low-pass filtering instrument time series with a cut-off period of 30 days. Thin horizontal lines indicate instrument depths, and the thick black contour shows the 34.94 isohaline, defining the top of the ISOW layer. White lines indicate isopycnals, with contour interval 0.025. Time tick marks are at the first day of every month. Two vertical black lines mark 2 September 2010 and 10 December 2011 (see later discussion). (b) Same as Figure 5a but for zonal speed. Thick black contour indicates the zero contour. Positive speeds are eastward.

Maximum mean salinities, 34.975, were observed in the NV, at the bottom instruments at moorings B and C. Lower salinity water, 34.920, near the bottom of the NV is colocated with the mean eastward current observed there (Figure 4b). Maximum mean ISOW salinity in the southern vein was lower than in the northern vein by about 0.02. The lower salinity LSW above the ISOW has a minimum salinity of 34.902 at mooring G at 1000 m ($\sigma\theta = 27.74$).

### 3.2. ISOW Transport Time Series and Mean Estimates

As a prelude to the discussion of ISOW transport observed with the B1012 array and comparison with S94, Figure 5 shows time-depth plots of zonal speed and salinity at mooring C, the tall mooring in the northern ISOW stream. The data have been low-pass filtered with a third-order Butterworth filter with a 30 day cut-off period, run forward and backward on the time series to eliminate any phase distortion. This was to remove high-frequency signals such as from possible topographic Rossby waves, evidence for which has been observed previously in the ISOW boundary current [*Schmitz and Hogg*, 1978; *Kanzow and Zenk*, 2014].

The most important feature to note in Figure 5 is that the thickness of the ISOW layer fluctuated by a factor of 2.5, from a minimum of ~700 m to a maximum of ~1700 m. These large fluctuations will be important when discussing differences between the S94 and B1012 mean ISOW transport estimates. Also note that zonal speed fluctuations above the ISOW layer were often positive when the ISOW layer was thin. In fact, there are several such occasions where nearly the entire water column up to 500 m was moving eastward—only the 3000 m current meter showed persistent westward flow at this mooring site. Finally, when ISOW layer thickness was low, there was usually anomalously fresher water above the ISOW, indicative of more recently ventilated LSW. These pulses of LSW are sometimes more weakly stratified (indicated by the density contours in the top figure).

#### 3.2.1. B1012 ISOW Transport Time Series and Mean Estimate

The 22 month time series of ISOW transport estimated daily from the B1012 array using the method described in section 2.2.2 is shown in Figure 6 by the thin black curve, with the thick black curve showing the low-pass filtered version (using a third-order Butterworth filter with a 30 day cut-off period, run forward and backward to eliminate phase shifts). As also observed by S94, the volume transport of ISOW during 2010–2012 exhibited strong temporal variability on multiple time scales, including complete reversals (i.e.,

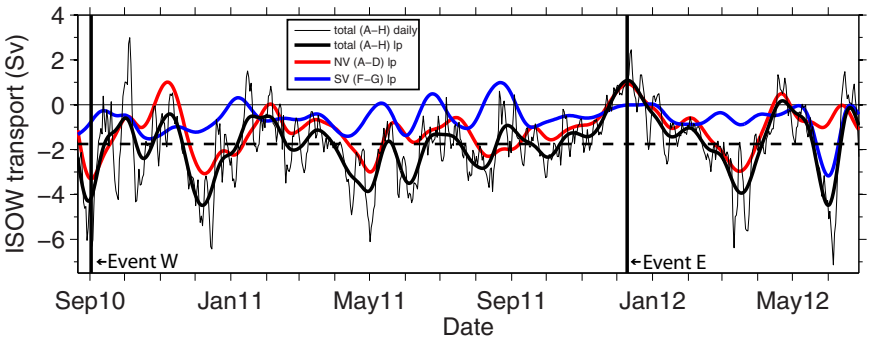


**Figure 6.** Time series of ISOW transport across the B1012 array. Thin black curve indicates daily mean total transport values, and thick black curve shows the 30 day low-pass filtered version. The dashed line denotes the record mean transport, −1.7 Sv. The red and blue curves show low-pass filtered transport in the NV (moorings A–D) and SV (moorings F and G), respectively. The two vertical lines mark dates that will be discussed later in the text (2 September 2010 and 10 December 2011).

eastward ISOW transport). Daily mean transport ranged from −7.1 to +3.0 Sv. The mean of daily ISOW transport estimates is $-1.7 \pm 0.5$ Sv, where the uncertainty is the 95% confidence interval around the mean, using an integral time scale of eight days (same as S94, and confirmed using the daily transport time series shown in Figure 6) to estimate degrees of freedom, 42, with the transport standard deviation of 1.6 Sv. S94 estimated a mean ISOW volume flux of $-2.4 \pm 1.2$ Sv (95% confidence interval estimated from S94's stated degrees of freedom, 25, and standard deviation, 3.0 Sv). These two estimates are not statistically different at the 95% confidence level, even though the B1012 mean estimate is 30% less than S94. This of course reflects the strong low-frequency variability in both time periods, the causes of which will be discussed in section 3.3.

Figure 7 shows the distribution of mean ISOW transport by mooring, and Table 2 lists the values with 95% confidence intervals. Mooring F, in the SV, has the single highest mean transport, but overall, the NV carries about twice as much ISOW as the SV, 66% versus 34%. This ratio is similar to what was found by S94 (60% and 40%). Furthermore, the total transport variability is dominated by the NV ISOW stream: the correlation coefficient between total and NV low-pass filtered transports (thick black and red curves in Figure 7) was $0.80 \pm 0.31$ versus $0.49 \pm 0.30$ between the total and SV transports (thick black and red curves in Figure 7). The strongest transport variability was observed at moorings D and G, i.e., at the deepest point of the two transform valleys, and the lowest was on the slope of the Reykjanes Ridge (moorings A and B) and at the southern-most mooring, H.

At all mooring sites, ISOW transport variability was influenced most by layer-averaged zonal speed fluctuations as opposed to layer thickness variations, as determined from correlation coefficients between transport and layer-averaged zonal speed. The correlation coefficients varied from $0.70 \pm 0.25$ (G) to $0.97 \pm$ (0.33, 0.50, and 0.27) (A, B, and D), indicating that positive velocity anomalies (eastward) are associated with positive transport anomalies (eastward). Correlation coefficients between transport and ISOW layer thickness were significantly less, and almost all negative (except at G), indicating generally that positive thickness anomalies (thicker layers) are associated with negative transport anomalies (stronger westward ISOW transport), as would be expected. Strongest correlations between ISOW transport and layer thickness were found at F ($-0.41 \pm 0.27$), A ($-0.33 \pm 0.20$), and B ($-0.30 \pm 0.17$). All uncertainties are 95% confidence intervals computed as described in Table 2.

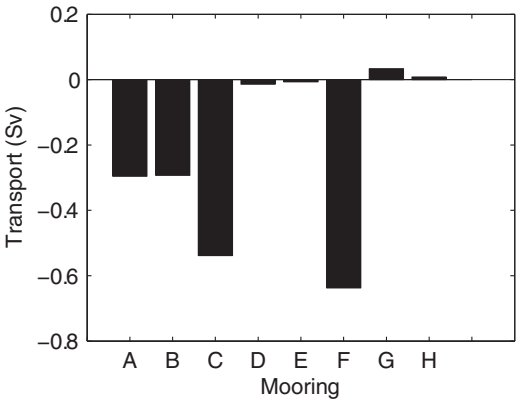


**Figure 7.** Mean ISOW transport through the CGFZ by mooring (north to the left). Numeric values also given in Table 2.

Figure 8 provides a compact summary of the low-pass filtered ISOW transport variability across the

**Table 2.** Mean ISOW Volume Transport (Left-Hand Side of Equation (1)) and the Eddy Component (Second Term on Right-Hand Side of Equation (1)), With 95% Confidence Intervals, for Each Mooring[a]

| Mooring Name | Mean Transport (Sv) | 95% (Sv) | Eddy Transport (Sv) | 95% (Sv) |
|---|---|---|---|---|
| A | −0.30 | 0.05 | −0.01 | 0.01 |
| B | −0.29 | 0.08 | −0.01 | 0.01 |
| C | −0.55 | 0.10 | 0.04 | 0.03 |
| D | −0.01 | 0.14 | −0.02 | 0.04 |
| E | −0.01 | 0.10 | −0.03 | 0.04 |
| F | −0.63 | 0.12 | 0.02 | 0.04 |
| G | 0.03 | 0.13 | −0.03 | 0.09 |
| H | 0.00 | 0.08 | −0.01 | 0.06 |

[a]Confidence intervals were estimated using bootstrap resampling on 10 day subsampled time series.

B1012 array in a time-latitude plot. At the northern end of the array (moorings A–C), ISOW transport was relatively steady in the westward direction, with only a few reversals. There was one major reversal at the end of 2011 that lasted for 34 days at mooring C (centered on the black vertical line in December 2011, here and in Figures 6 and 7), and which impacted the other mooring sites in the northern part of the array. For example, the persistent eastward event centered at the end of 2011 lasted for about four months at mooring D. This major event will be discussed more below. In the southern half of the NV (moorings D and E), transport variability was significantly greater, and there were frequent reversals in transport direction. In fact, ISOW transport was as likely to be eastward as westward at these sites.

In the SV, mooring F exhibited relatively persistent westward ISOW transport, with reversals only about 3% of the time. Transport at mooring G on the other hand, at the axis of the SV, was highly variable and ISOW transport was westward 41% of the time. Also evident in Figure 8 is the break in coherence in transport variations across the median ridge (located between moorings E and F): the correlation coefficient between the two ISOW transport streams (moorings A–D versus F and G) was $-0.05 \pm 0.20$ at zero lag (see also Figure 6). Maximum lagged correlation, $0.21 \pm 0.17$, occurred when SV transport led by 32 days, reflecting some northward propagation, especially obvious in August–September 2011.

### 3.2.2. Comparison Between Saunders [1994] and B1012 Mean ISOW Transport Estimates

Some results presented above suggest that there could be an issue in the S94 mean ISOW transport estimate as a result of using a fixed ISOW layer thickness in the transport calculation. In essence, S94 made two (necessary) assumptions by using a fixed ISOW layer thickness: (1) that speed and thickness fluctuations are uncorrelated, i.e., eddy volume transports (second term on right-hand side of equation (1)) are small compared to the transport of ISOW associated with the mean current acting on the mean layer thickness (first term on right-hand side of equation (1)) and (2) the thickness estimates obtained from the single CTD section were representative of the mean during the mooring deployment:

$$\overline{Uh} = \overline{U} \cdot \overline{h} + \overline{U'h'} \tag{1}$$

where $U$ is the layer-averaged zonal speed, $h$ is the ISOW layer thickness, and overbars indicate time averages and primes denote fluctuations from the time mean.

The first assumption is easily tested with the B1012 array observations. We find very low correlation coefficients between layer-averaged zonal speed and layer thickness, the result being small eddy transport

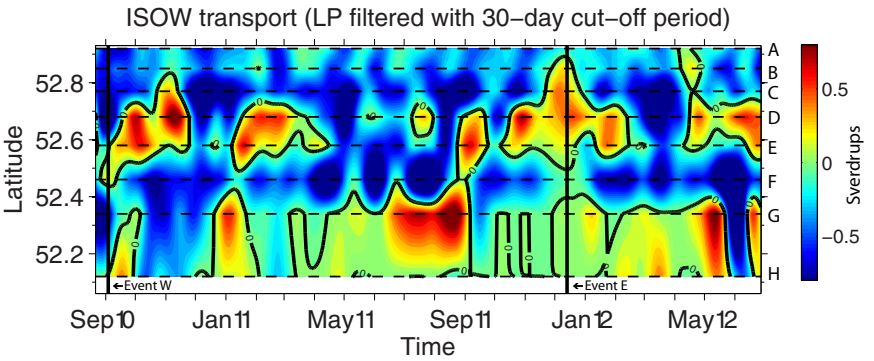


**Figure 8.** Time-latitude plot of ISOW transport (low-pass filtered with 30 day cut-off period). Dashed lines indicate mooring latitudes (labeled on right axis), and thick black contour shows zero transport. The two vertical black lines mark dates that are discussed in the text (2 September 2010 and 10 December 2011).

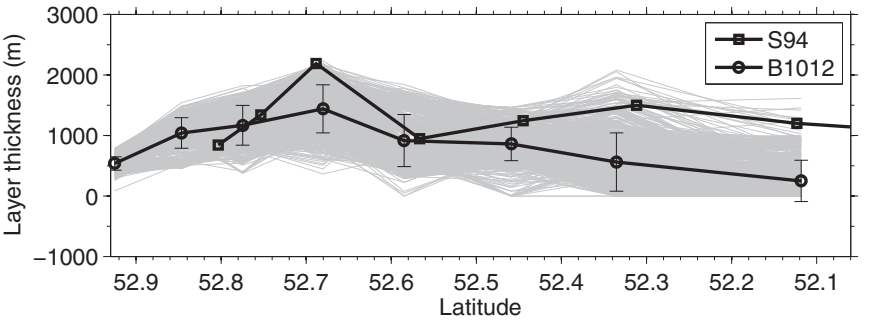


**Figure 9.** ISOW layer thickness as a function of latitude (north on the left). Gray lines show daily values from B1012, circles connected by a black line indicate mean and standard deviation at each mooring site. Squares connected by a black line show ISOW layer thickness from S94 CTD profiles at the time of his mooring deployment cruise, based on his Figure 2.

estimates that are generally not distinguishable from zero (Table 2). Therefore, it appears that S94's implicit assumption that eddy transports do not contribute significantly to the mean zonal ISOW transport through CGFZ is valid.

The second assumption regarding use of a single snapshot of the salinity distribution to represent the mean is more difficult to test because we have no other information about the salinity distribution during 1988–1989. We can say, however, that the S94 salinity snapshot is not representative of the mean during the B1012 time period. Figure 9 shows daily and mean ISOW layer thickness as a function of latitude/mooring for the B1012 observations, and from S94's CTD section (from his Figure 2). S94's layer thickness is greater than the B1012 2 year mean at almost every site across the CGFZ, although it is within the range of the B1012 daily values. The cross-array mean ISOW thickness was 1270 m for S94, while for the new observations it was 846 m, or 33% thinner. This is similar to the 30% lower mean transport using the B1012 array. While it cannot be proven, these results suggest that the S94 mean ISOW transport estimate may have been an overestimate due to the use of a synoptic salinity section to estimate ISOW layer thickness. Perhaps the larger point here though is that zonal ISOW transport through the CGFZ is highly variable and means derived from 1 to 2 year long time series cannot be statistically distinguished. In the following subsection, the causes of this variability will be investigated in more detail.

### 3.3. The North Atlantic Current's Impact on ISOW Transport Through the CGFZ

#### 3.3.1. Velocity and Salinity Structure During Extreme ISOW Transport Events

Being the first to document the strong mesoscale variability in ISOW transport through the CGFZ, S94 suggested the nearby NAC as one potential cause. *Schott et al.* [1999] furthered this argument with a single LADCP section across the CGFZ that showed all eastward flow in August 1997. One of the primary objectives of the B1012 array was to investigate the impact of the NAC on ISOW transport by simultaneously observing deep and upper ocean currents continuously for an extended time period. We also have the advantage of remote sensing products at our disposal with which to characterize the surface circulation patterns during 2010–2012.

We begin by illustrating the circulation and salinity distribution during minimum and maximum ISOW transport events in the 2010–2012 time period. More precisely, we highlight the structures during minimum and maximum transport events *in the NV* because (1) it dominates the total ISOW transport mean and variability and (2) it is uncorrelated with transport variability in the SV. Equivalent figures for extreme transport events in the SV are provided in the supporting information.

Figure 10a shows the AVISO map of absolute dynamic topography (ADT) for 2 September 2010, when low-pass filtered ISOW transport in the NV (moorings A–D) was relatively strong to the west (−3.3 Sv, "Event W"; see Figures 6 and 8). Overall, it shows a meandering NAC crossing the MAR, as well as many closed eddies. The northernmost current branch was approaching the MAR between 51.5°N and 52°N. At the array longitude, the main body of the current branch was entirely south of mooring H and the ADT gradient was near zero across the array. The 500 m currents (red vectors) were westward in the north, and mostly southward in the south, while 3000 m (or bottom at moorings A and B) currents at most mooring sites had a strong westward component, reaching a maximum westward current of −16 cm/s at mooring A. The cross section

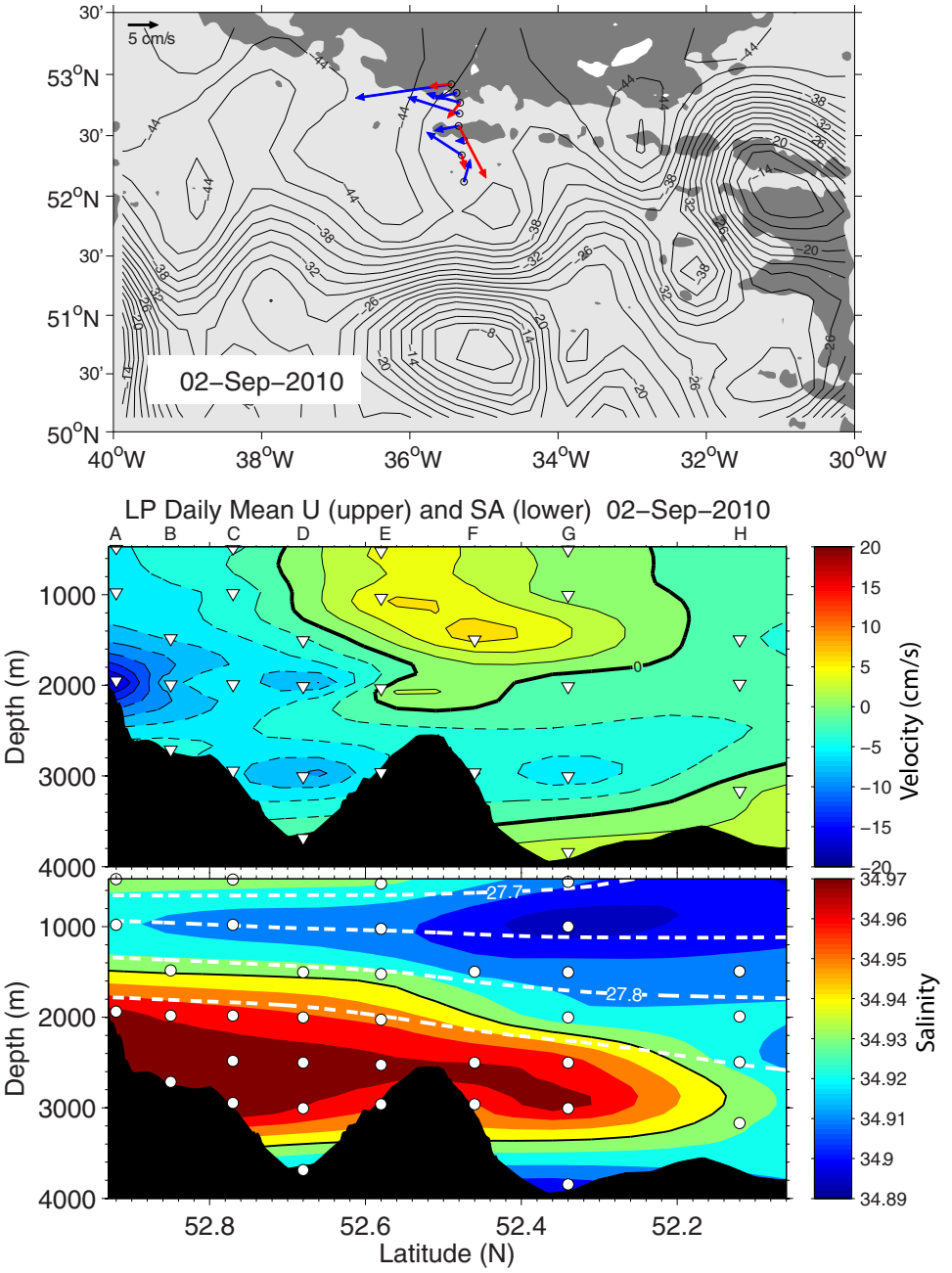


**Figure 10.** (a) Map of ADT for 2 September 2010, when NV ISOW transport was relatively strong to the west. ADT is contoured every 2 dynamic cm. Blue vectors show daily mean low-pass filtered velocity at the bottom instrument (moorings A and B) or 3000 m (moorings C–H), and red vectors show the same at 500 m at moorings A, C, E, and G), on the same day as the ADT map. (b) Daily mean low-pass filtered zonal speed and (c) salinity from B1012 array for the same date. Refer to vertical black line ("Event W") in Figures 6 and 8 to place this date in context with the total and NV transport time series.

of low-pass filtered zonal speed on the same date reveals westward flow everywhere except in the very bottom of the two transform valleys, and at depths 1500 m and above at moorings E–G. (Figure 10b). The high-salinity ISOW layer was relatively extended toward the south, and the freshest LSW was observed at the southern moorings (Figure 10c).

In contrast, conditions during a strong *eastward* NV ISOW transport event are illustrated in Figure 11, which shows the same variables as in Figure 10 but for 10 December 2011, when NV ISOW transport was +0.9 Sv (see "Event E" Figure 6). The ADT map indicates that at this time, a branch of the NAC was flowing eastward

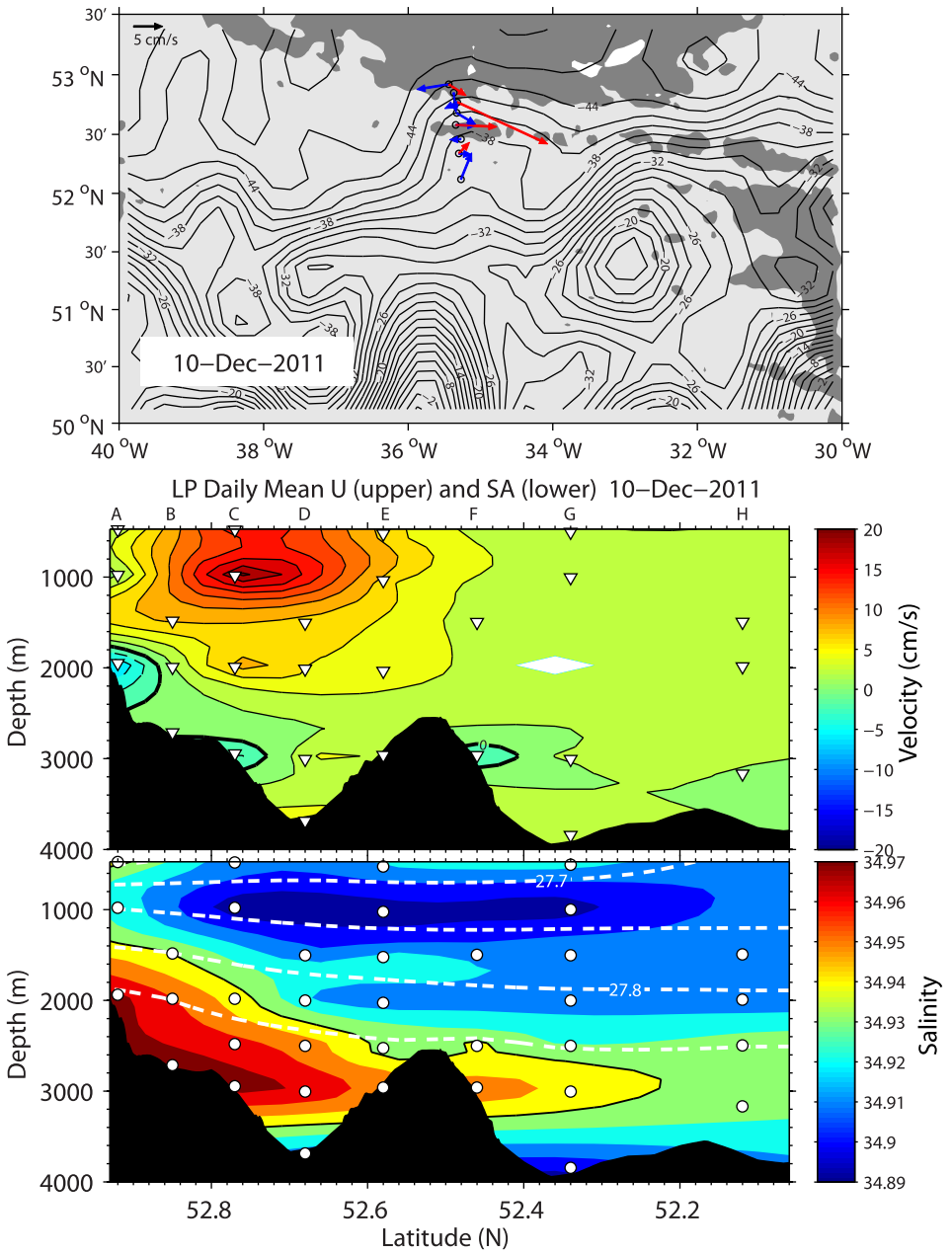


**Figure 11.** Same as for Figure 10 but on 10 December 2011, when NV ISOW transport was to the east. Refer to vertical black line in Figures 6 and 8 ("Event E") to place this date in the context of the full transport time series.

over the mooring array. All four 500 m current meters showed an eastward component, with a maximum zonal speed of 15 cm/s at mooring C (Figure 11b). The vertical section of zonal speed indicates a strong eastward jet over the NV (Figure 11b), with a maximum of 20 cm/s at the 1000 m instrument at mooring C. Westward flow in the ISOW layer is much weaker than in Figure 10b, and confined to the bottom instruments at moorings A, C, and F. The high-salinity ISOW layer was more contracted to the north than in the previous example, and the fresher LSW had shifted northward (Figure 11c). The ISOW layer was thinner and fresher at moorings C–G, suggesting that the eastward current was advecting less saline ISOW past the moorings. The salinity changes evident in this eastward event were not common to all eastward events, see below.

The configuration of the surface currents inferred from gradients of ADT during these two examples is very similar to that during other extreme NV ISOW transport events. Figure 12a shows the NAC position for six

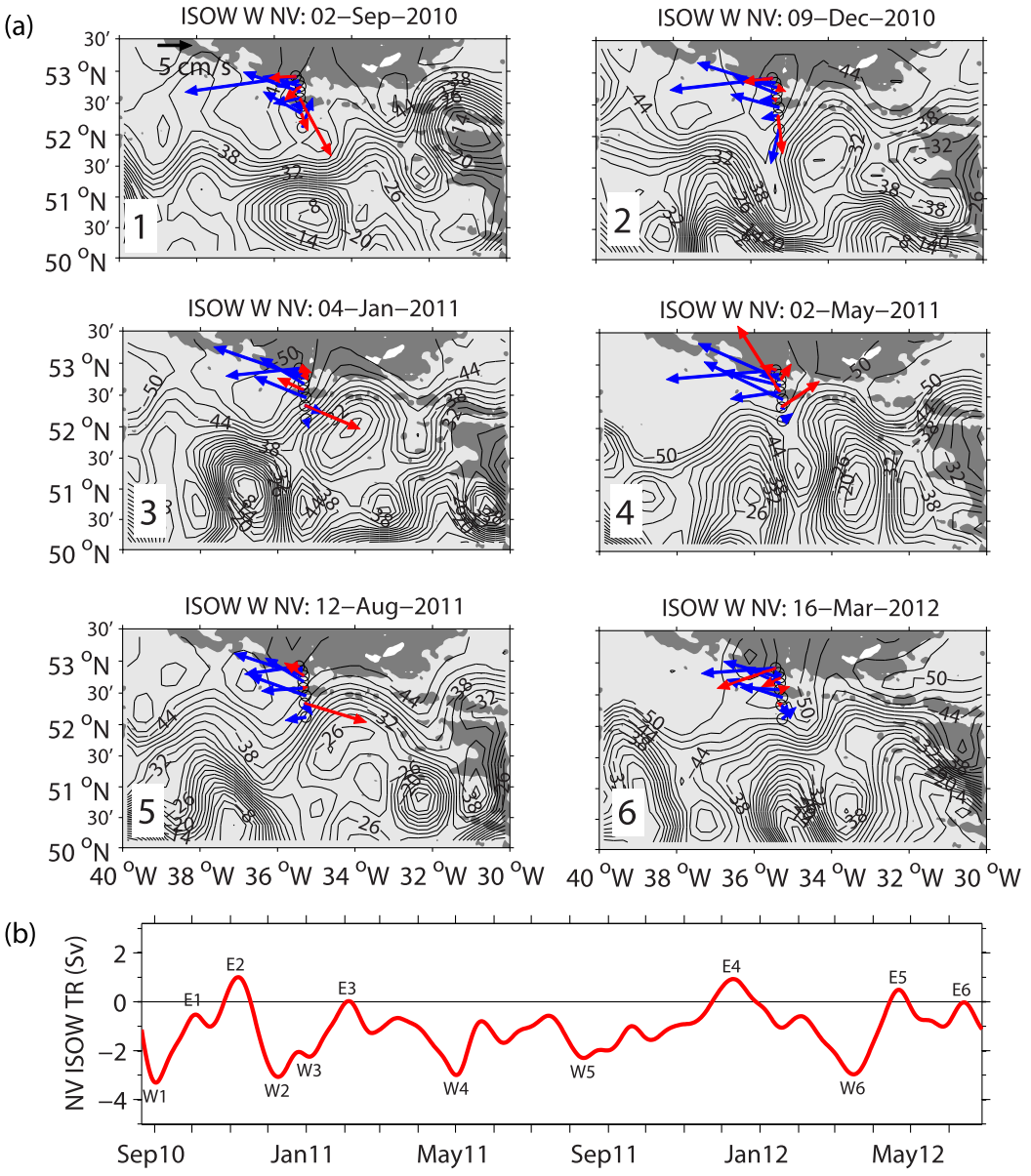


**Figure 12.** (a) Maps of ADT for the six strongest westward NV ISOW transport events. ADT and bathymetry are presented as in Figure 10. (b) Time series of NV ISOW transport (from Figure 6) showing when each westward ("W") and eastward ("E") event took place in the context of the full NV ISOW transport time series. ADT maps for the six events marked with "E" are presented in Figure 13.

events with maximum low-pass filtered westward NV ISOW transport in the NV, including the highlighted example above (Event 1), along with the NV ISOW transport time series where each event is marked with the corresponding event number (Figure 12b; W1–W6). These snapshots share a common characteristic in that the NAC was located near or south of the southern moorings and ADT gradients were very weak over the *northern* part of the B1012 array. This contrasts with the six events with the most easterly NV ISOW transport, Figure 13, when ADT gradients were generally (but not always) stronger over all or some of the mooring array. These events are labeled E1–E6 in Figure 12b. Exact correspondence between the NAC branch positions from ADT and the mooring observations cannot be expected since the ADT maps provide a smoothed (in space and time) picture of the NAC branches, while the zonal speed cross sections above (Figures 10b and 11b) reveal that the meridional scales of the zonal flows can be quite small, and may not always be well resolved in satellite-derived ADT.

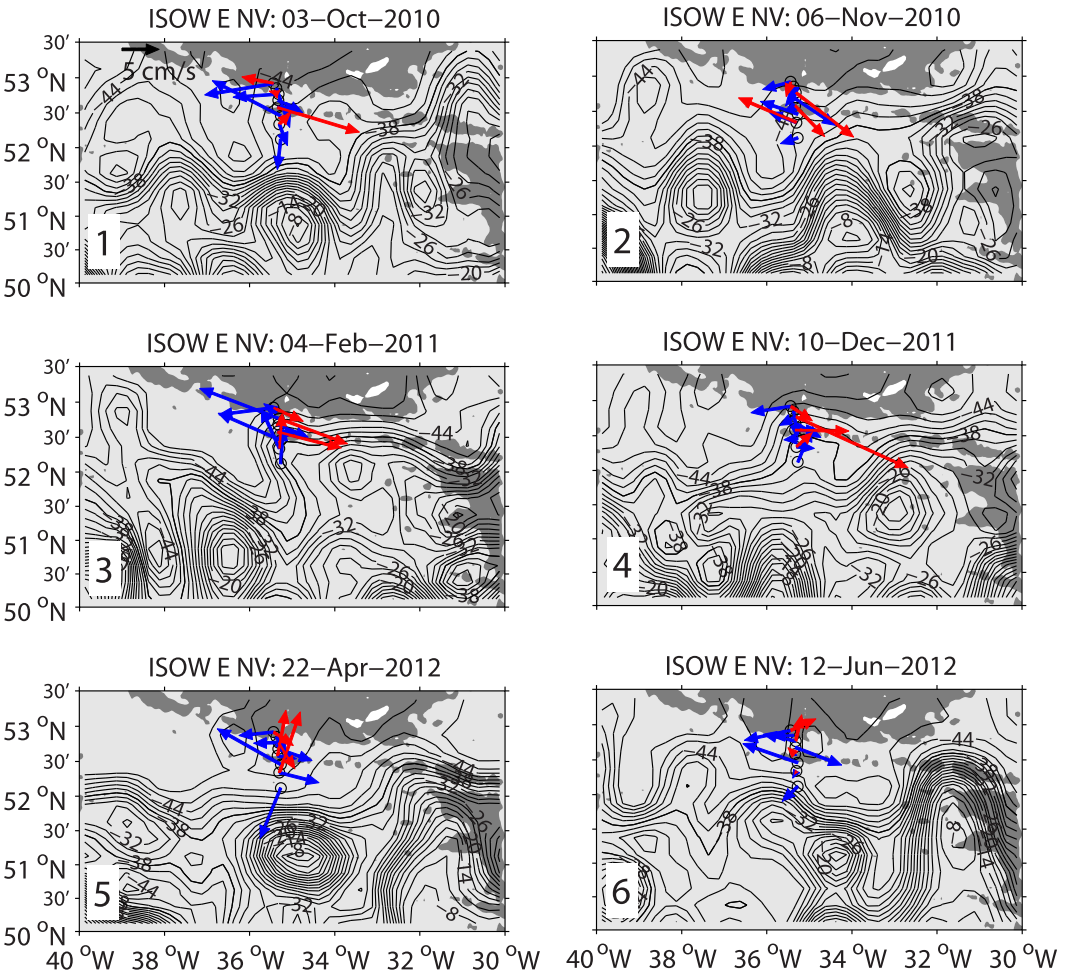


**Figure 13.** Same as for Figure 12 but for the six weakest (or eastward) NV ISOW transport events. Refer to Figure 12b for "E" events in time series.

The surface and subsurface structural differences between minimum and maximum NV ISOW transport states are summarized in Figure 14, which shows composites of ADT, zonal speed and salinity for the six extremes of each sign. On average, meridional ADT gradients over the array were stronger during eastward events compared to westward events. This pattern extends below the surface, where zonal speed was more strongly eastward over the NV when NV ISOW transport was positive or weakly negative (circled instruments show which composite means are statistically significantly different at the 95% confidence interval). The ISOW layer was slightly more saline and thicker *in the NV* during westward events, but the differences do not pass the 95% confidence level at most instruments.

A similar set of figures but for ISOW transport extremes in the SV can be found in the supporting information, including snapshots of ADT and salinity and zonal speed sections for relatively strong westward (supporting information Figure S1) and eastward (supporting information Figure S2) SV ISOW transport events. ADT maps for the six strongest SV ISOW transport events and six strongest eastward SV ISOW events are shown in supporting information Figures S3 and S4, respectively, and composites are provided in supporting information Figures S5. The story is very similar as for the NV transport reversals: stronger meridional ADT gradients over the SV during Eastward SV ISOW transport events, a stronger eastward jet over the SV (again, with a maximum at 1000 m) and a more saline ISOW layer in the SV (with a similar pattern of statistical significance in the differences). Together with the NV results, these figures point to the NAC as the primary cause of low-frequency variability in ISOW transport through the CGFZ, with the strongest NAC influence observed over the deepest parts of the CGFZ.

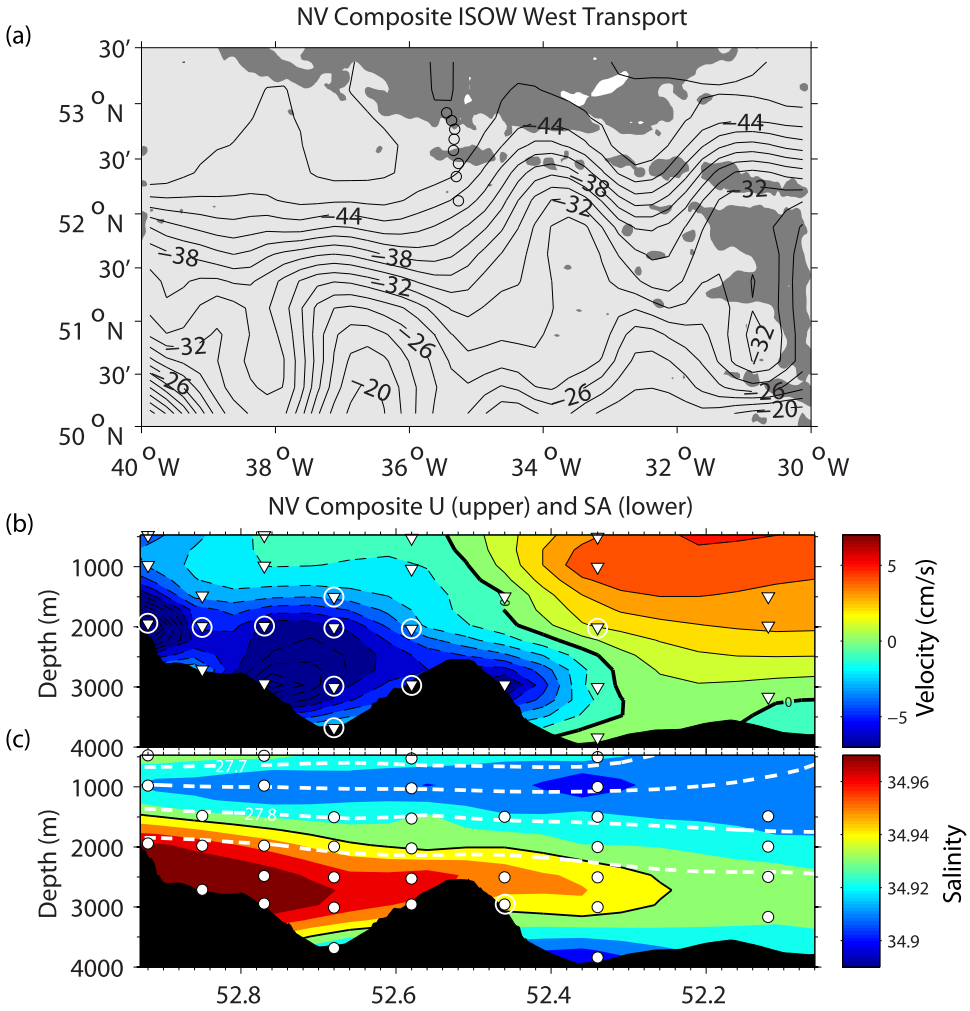


**Figure 14.** (a–c) Composites of ADT, zonal speed, and salinity for the six strong westward NV ISOW transport events. Individual ADT maps for the six events included in the composite are shown in Figure 12. Circles indicate instruments where westward and eastward composite mean values are statistically different at the 95% confidence level. (d–f) Same as in Figures 14a–14c except for the six eastward or weak westward NV ISOW transport. Individual ADT maps for the six days are shown in Figure 13. Equivalent figures for westward and eastward SV ISOW transport events are provided in supporting information Figure S5.

The lack of statistical significance in the composite water property distributions between strong westward and weak westward (or eastward) ISOW transport is curious. One might expect that the reversals in the velocity field result in a systematic oscillation of water properties passing the B1012 array. This would be the case if the ISOW water property distribution is characterized by a high-salinity ISOW reservoir east of the CGFZ and a lower salinity ISOW reservoir to the west (the product of vertical and lateral mixing in the fracture zone) [*Yashayaev and Dickson*, 2008]. In this conceptual model, eastward flow perturbations would be accompanied by decreasing salinity. However, this is not captured in the mean composites above (Figure 14). This may be because after a period of westward flow of high-salinity water followed by a flow reversal, the same water that flowed past the moorings going westward will pass by again going eastward, modified or not modified depending on the mixing intensity and time scale of the reversals. This may particularly be the case in the more bathymetrically constrained NV. Furthermore, inhomogeneity's in the water properties east and west of the fracture zone will introduce more property variability at the moorings that is independent of the flow direction (e.g., see Figure 5).

These complexities are illustrated in Figure 15, which shows low-pass filtered zonal speed (blue) and salinity (green) at the 3000 m instruments on moorings D and G. These moorings, positioned in the deep troughs of the NV and SV, were chosen because the zonal speed here frequently reversed direction. There are several episodes where an eastward velocity anomaly is accompanied by decreasing salinity (in quadrature) as

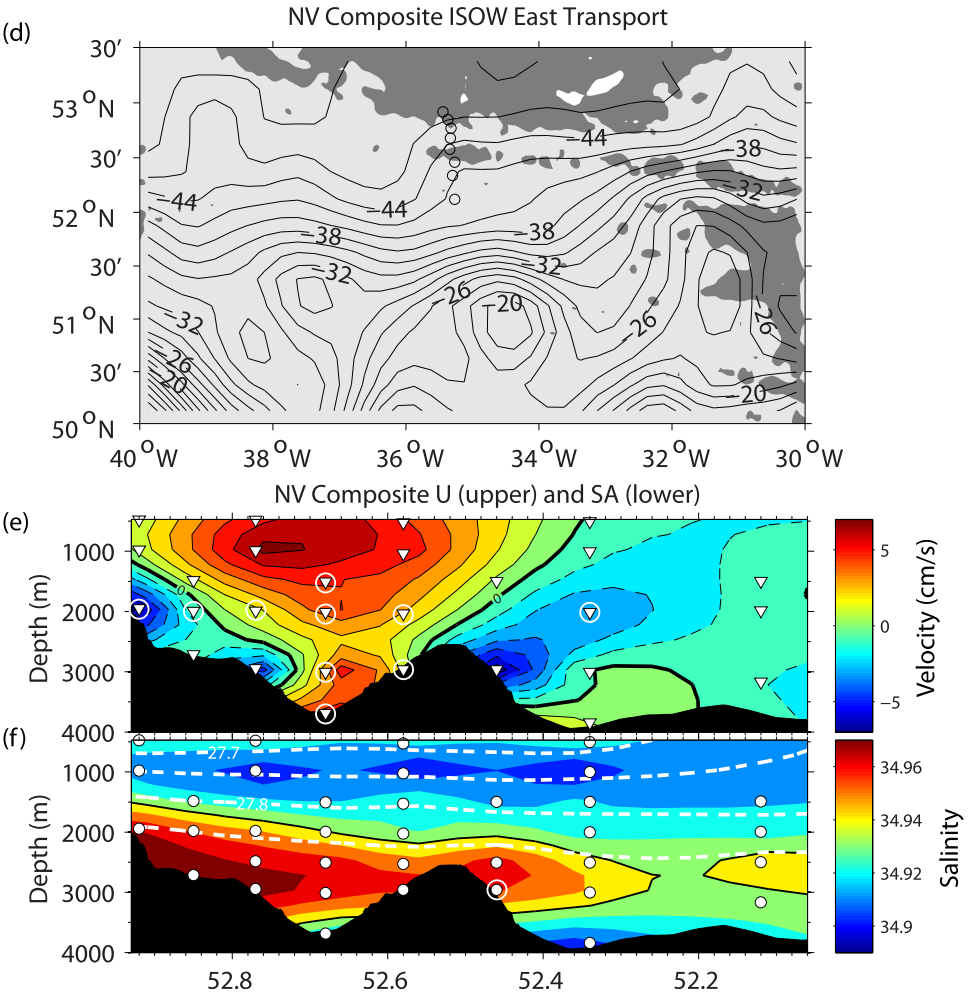


**Figure 14.** (continued)

described in the conceptual model (e.g., November 2010, July 2011, and December 2011), and similarly to some extent at mooring G (the series of positive velocity anomalies beginning in December 2011). However, there are other time periods when a different relationship between the tendencies of zonal speed and salinity was observed, especially at mooring G (January 2011 and June 2012), where the lack of a southern wall likely allows more isotropic stirring. These results help to explain the lack of a significant difference in water properties in the composite means (Figures 14c and 14f and supporting information Figures S5c and S5f), and highlight the complex interplay of currents and water properties in the deep CGFZ, a topic worthy of a dedicated study.

### 3.3.2. EOF Vertical Modes and ISOW Transport

We further explore the relationship between the NAC and ISOW transport variability by computing the EOFs for zonal speed at each of the tall moorings (A, C, E, and G) and comparing the principle components (PCs) to the ISOW transport time series. Table 3 lists the fraction of total variance explained by the first three EOFs, and Figure 16 shows the vertical structure of these modes for each of the tall moorings. The first mode explains 68–74% of the variance, and its vertical structure is unidirectional at all four sites. At the three deepest locations (moorings C, E, and G), it has a slight maximum at the 1000 m instrument, and amplitude decreases with increasing depth. The second mode explains 21–27% of the variance and has a single zero crossing at each mooring, between 1000 and 2000 m at moorings A, C, and E, and between 2000 and 3000 m at mooring G. Vertical shear of this mode was all below 1000 m. The zero crossing of this mode may be following the interface between LSW and ISOW, but this cannot be confirmed without

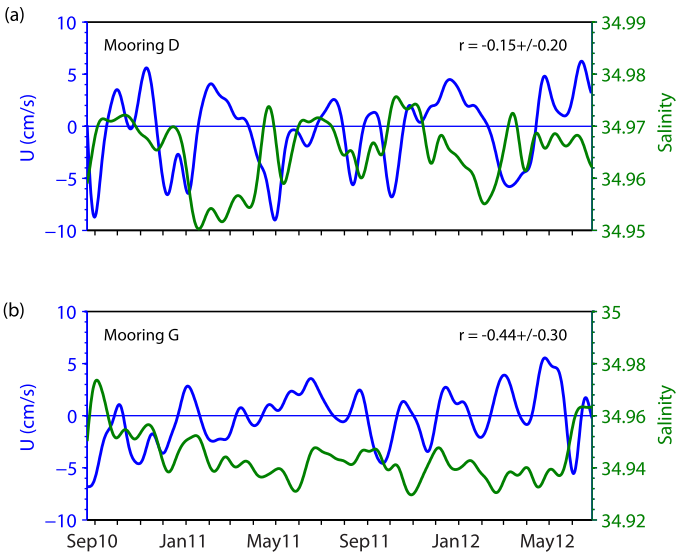


**Figure 15.** Time series of low-pass filtered zonal velocity and salinity for the 3000 m instruments at (a) mooring D and (b) mooring G. The correlation coefficient and its 95% confidence interval between the two time series at each mooring is in the right top corner of each figure.

higher-resolution vertical profiles of salinity and velocity. Mode 3, explaining only 3–6% of the variance, has two zero crossings, with the middepth extremum increasing in depth from mooring A to G.

The PCs are similar for all four moorings, so they are shown only for mooring C in Figure 16. The PC for Mode 1 (Figure 17a) is dominated by lower frequencies than the other modes, and is negative (westward anomaly) for Event W and positive (eastward anomaly) for Event E, consistent with the results above. The PCs for modes 2 and 3 (Figures 17b and 17c) do not appear to have extrema associated with the ISOW transport minimum and maximum events.

The covariation of mode 1 and ISOW transport is illustrated in Figure 18, which shows PC1 and mooring-specific ISOW transport for each of the four tall moorings. Both time series have been low-pass filtered with a 30 day cut-off period. These two quantities are not entirely independent, since the transport calculation includes the vertically averaged zonal speed over the ISOW layer. However, the high correlations between these time series, 0.65–0.83 (Table 4), indicate that the variability in ISOW transport is strongly related to current fluctuations that are unidirectional throughout the water column rather than with a higher mode variability associated with, for example, surges in the ISOW layer alone. Correlation coefficients between ISOW transport and PC2 and PC3 (Table 4) point to the secondary importance of more baroclinic processes at moorings C, E, and G in modulating the ISOW transport. At mooring A, the correlation coefficients between ISOW transport and PCs are about the same for PC1 and PC2, even though mode 1 explains more than twice as much of the variance as mode 2. This suggests that surges of the ISOW layer, though less energetic than the barotropic velocity fluctuations at mooring A, also modulate ISOW transport variability at this location. This difference from the other sites is consistent with its location higher up on the slope, where it is more difficult for the deep-reaching

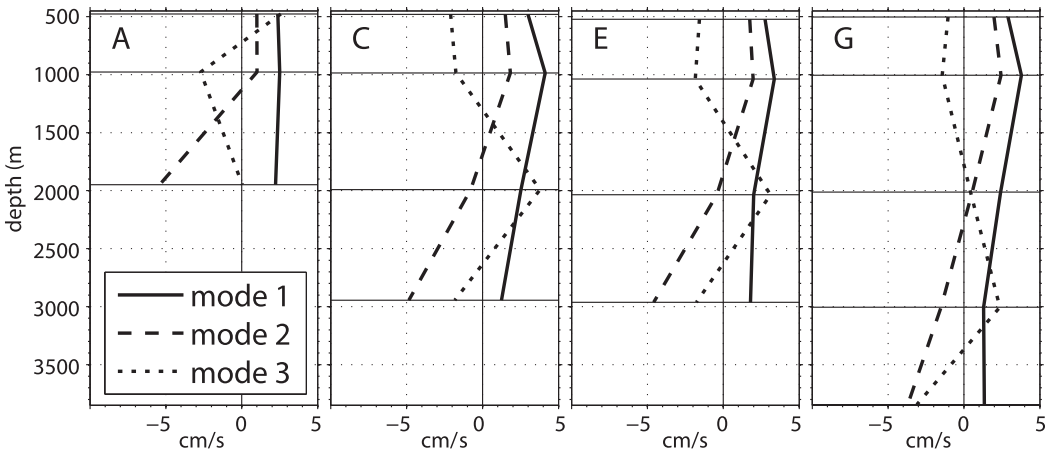


**Figure 16.** First three EOF modes at each of the four tall (i.e., extending up to 500 m) B1012 moorings. The nondimensional mode amplitudes have been renormalized with the standard deviation at each instrument, giving units of cm/s. (a) Mooring A, (b) mooring C, (c) mooring E, and (d) mooring G. Horizontal lines indicate depths of current meters used in the calculation of the EOFs. Fraction of total variance explained by each mode at each mooring site is given in Table 3.

**Table 3.** Fraction of Total Variance Explained by EOF Modes 1–3 at the Four Tall Mooring Sites

| Mode | A | C | E | G |
|---|---|---|---|---|
| 1 | 0.70 | 0.68 | 0.74 | 0.69 |
| 2 | 0.27 | 0.25 | 0.25 | 0.21 |
| 3 | 0.03 | 0.06 | 0.04 | 0.06 |

velocity fluctuations associated with the NAC to penetrate. The physical processes associated with modes 2 and 3 warrants further research.

## 4. Summary and Discussion

A nearly 2 year mooring array (called B1012) was deployed across the CGFZ from August 2010 to June 2012 to measure the transport of ISOW through this deep gap in the MAR and investigate causes of its low-frequency variability. The B1012 array was enhanced compared to an earlier study (S94) with the addition of a mooring higher up on the slope of the Reykjanes Ridge, sensors extending up to 500 m depth, and the addition of microcat CTDs to continuously measure salinity as well as temperature.

The mean zonal velocity structure determined from the B1012 array measurements below 2500 m depth was similar to that reported by S94 in several ways. Seemingly separate streams or veins of ISOW flow westward through the two transform valleys of the CGFZ, both banked up against the northern slopes of the valleys, up to at least the 2000 m isobath in the case of the NV. Maximum westward speeds were 6–8 cm/s at the bottom instruments. Mean salinity was higher in the northern valley. Unlike S94, the B1012 array observations showed a narrower westward ISOW vein in the NV, and stronger eastward mean currents transporting fresher waters at the bottom of both transform valleys. The deep eastward mean flow in the NV was banked up against the northern wall of the median ridge, suggestive of an eastward deep boundary current transporting LDW into the eastern basin.

Following S94 and using the 34.94 isohaline as the boundary between ISOW and fresher water masses above and below, but using time-dependent ISOW layer thickness, the B1012 measurements give a (677

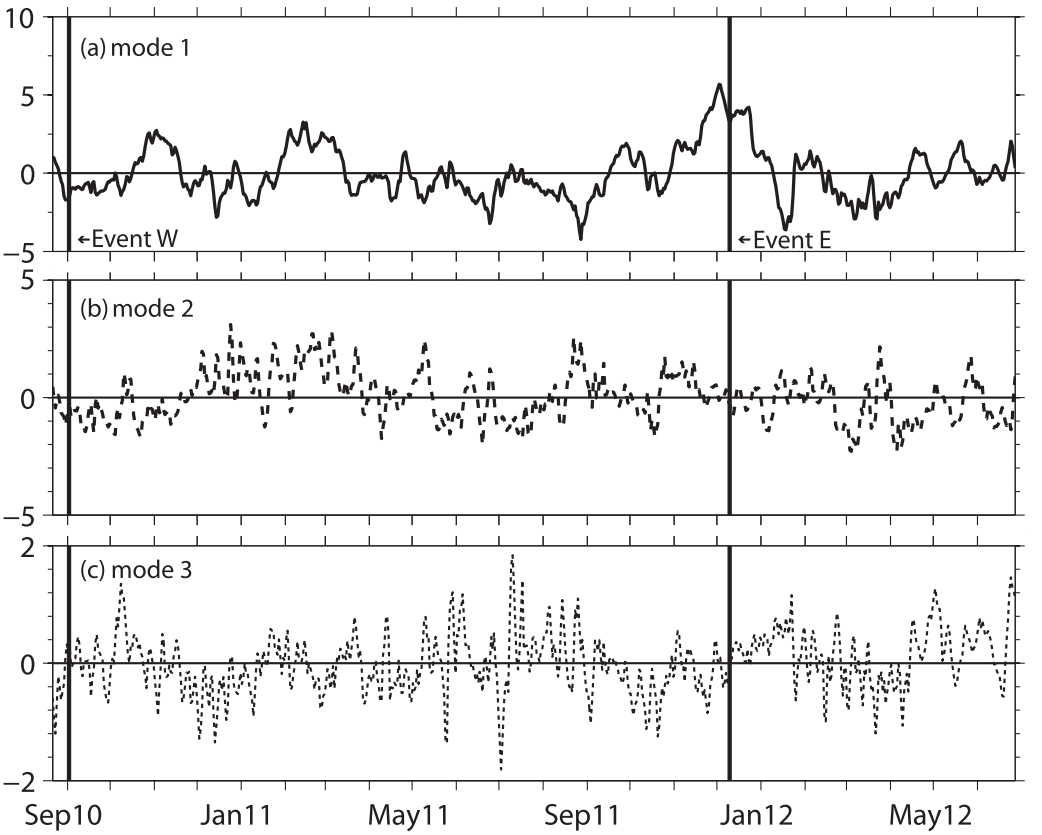


**Figure 17.** Principal components (PC) for the first three EOF modes at mooring C. Mode structure is shown in Figure 15b. (a) PC1, (b) PC2, and (c) PC3. The two vertical black lines mark dates of strong westward ISOW transport in the NV (2 September 2010, Event W) and eastward ISOW transport in the NV (10 December 2011, Event E), shown in detail in Figures 10 and 11, respectively.

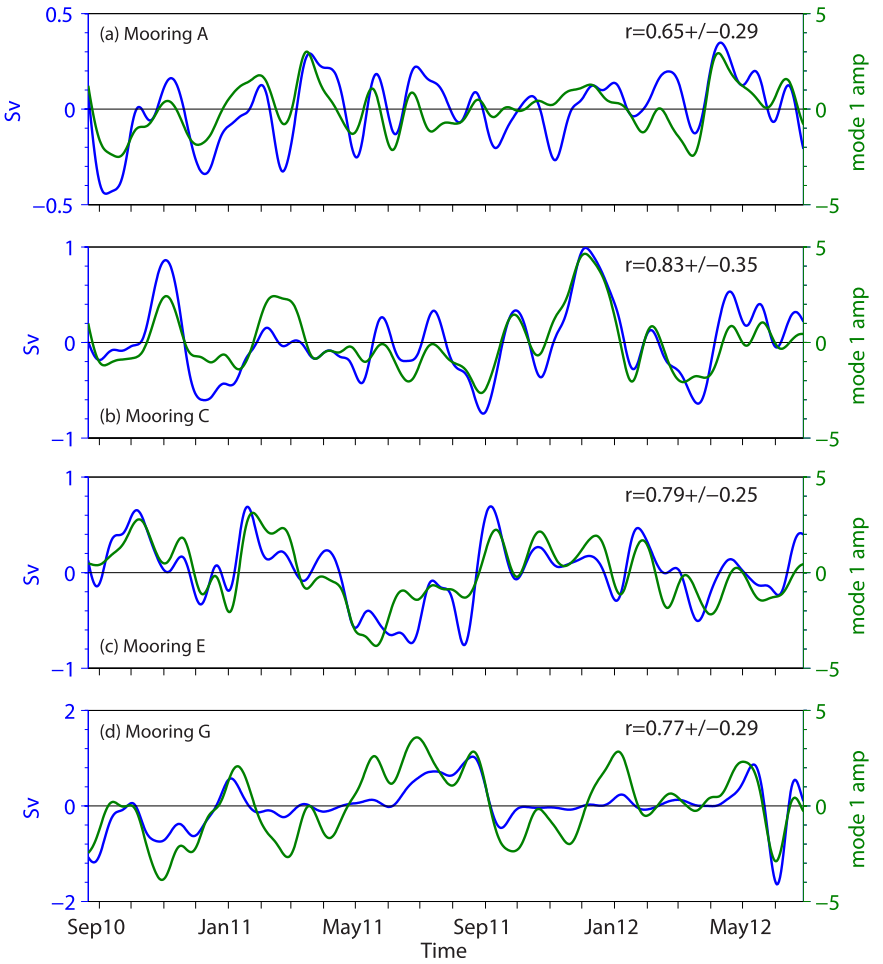


**Figure 18.** Time series of low-pass filtered PC1 and ISOW transport at each tall mooring site. The correlation coefficient and its 95% confidence interval between the two time series at each mooring is in the right top corner of each figure. (a) Mooring A, (b) mooring C, (c) mooring E, and (d) mooring G. Correlation coefficients and their 95% confidence interval between ISOW transport and all three principal components are given in Table 4.

days) mean ISOW transport of $-1.7 \pm 0.5$ Sv (95% confidence interval), which is 30% lower than S94's record (400 days) mean value of $-2.4 \pm 1.2$ Sv. Like S94, mean ISOW transport through the northern valley accounted for about 2/3 of the total, and transport variability was highest over the deepest parts of both valleys. ISOW transports in the two CGFZ valleys were uncorrelated, as also found by S94. Variability in the total ISOW transport is mainly driven by transport variations in the NV.

One possible explanation for the difference in mean ISOW transport between S94 and B1012 was found to be S94's use of a time-invariant ISOW layer thickness estimated from a CTD section at the time of mooring deployment, necessitated by the lack of salinity sensors on his moorings. Mean ISOW layer thickness obtained from continuous salinity measurements was 33% thinner than S94's estimate, although the latter was within the range of daily layer thickness observed with B1012. This difference is of the same order as the difference in mean ISOW transport, 30%, suggesting that S94's mean ISOW transport was overestimated.

**Table 4.** Correlation Coefficients and Their 95% Confidence Interval Between Low-Pass Filtered ISOW Transport and Principal Components for First Three EOF Modes at Each Mooring

| Mooring | r1 | r2 | r3 |
|---|---|---|---|
| A | $0.65 \pm 0.29$ | $-0.62 \pm 0.22$ | $0.03 \pm 0.22$ |
| C | $0.83 \pm 0.35$ | $-0.35 \pm 0.20$ | $0.29 \pm 0.22$ |
| E | $0.79 \pm 0.25$ | $-0.25 \pm 0.27$ | $0.11 \pm 0.09$ |
| G | $0.77 \pm 0.29$ | $0.10 \pm 0.24$ | $0.32 \pm 0.38$ |

Following up on suggestions by S94 and *Schott et al.* [1999] that the large variability in ISOW transport through the CGFZ is related to meanders of the NAC, maps of ADT were used to

determine the approximate position of the surface currents at the times of ISOW transport extrema, and it was found that when ISOW transport was weakly westward or reversed (eastward), it was typical for there to be strong zonal surface currents over all or part of the array associated with northward excursions of the NAC. The mooring observations support this interpretation—eastward zonal jets were observed over the transform valleys during episodes of weak westward or eastward ISOW transport. The ISOW layer was slightly more saline and thicker during strong westward ISOW transport, but not significantly so, probably due to a complex relationship between water properties and flow direction in the CGFZ. These results confirm earlier suggestions that deep-reaching meanders and/or eddies associated with the NAC are responsible for the energetic mesoscale variability in ISOW transport through the CGFZ.

EOF analysis of the zonal speed at the four tall moorings, i.e., with instruments extending up to 500 m depth, indicated that 68–74% of the total variance was explained by the first EOF mode, whose vertical structure was unidirectional with weak vertical shear above and below 1000 m depth at the three deepest tall moorings. The principal components for mode 1 were dominated by lower frequencies compared to modes 2 and 3 and were significantly correlated with ISOW transport variability. Although less energetic, surges in the ISOW layer were also significantly correlated with ISOW transport higher up on the slope of the Reykjanes Ridge. These results indicate that the ISOW transport variability is mainly controlled by fluctuations in zonal speed that extend throughout the whole water column, and secondarily by baroclinic processes, perhaps including surges of the ISOW layer.

With these results in mind, we revisit some previous works on the circulation of ISOW in the subpolar North Atlantic. In their review of ISOW transport estimates in the Iceland Basin, *Kanzow and Zenk* [2014] pointed out the need to better constrain ISOW transport along pathways around and out of the basin. This was highlighted by the significant difference between their estimate of −3.8 Sv south of Iceland near 61°N, and S94's −2.4 Sv through the CGFZ.

The lower mean ISOW transport estimate through the CGFZ reported here strengthens Kanzow and Zenk's point that there must be other major ISOW pathways out of the Iceland Basin that have not been quantified, and which together may equal the flux through the CGFZ. For example, there is growing evidence for ISOW transport through other gaps in the Reykjanes Ridge north of the CGFZ, and specifically the deepest of these, the Bight Fracture Zone (BFZ) near 57°N, Figure 1 [*McCartney*, 1992; *Bower et al*., 2002; *Lankhorst and Zenk*, 2006; *Xu et al*., 2010; *Kanzow and Zenk*, 2014; *Daniault et al*., 2016]. There are also several studies showing some ISOW transport continuing southward past the entrance to the CGFZ and along the eastern flank of the MAR [*van Aken*, 2000; *Fleischmann et al*., 2001; *Lankhorst and Zenk*, 2006]. Where this path ends up is unknown. Clearly more attention is needed to quantify the pathways of ISOW through and out of the Iceland Basin.

Historical hydrographic observations throughout the subpolar North Atlantic have been used to show the decrease in ISOW salinity as it mixes with LSW and DSOW along its path from its source in the Iceland Basin to the Labrador Sea [*Yashayaev and Dickson*, 2008]. These authors showed that there is a stepwise decrease in ISOW salinity in the CGFZ. This hydrographic evidence is consistent with the results presented here showing strong interaction between the ISOW and NAC in the CGFZ, which likely contributes to the stirring and mixing of ISOW with surrounding waters, including LSW and LDW.

What might be the impact of ISOW-NAC interaction in the CGFZ on the downstream path of ISOW? Several authors have depicted ISOW turning northward after exiting the CGFZ and continuing as a boundary current around the Irminger Basin before intersecting with the outflow from the Denmark Strait [e.g., *Dickson and Brown*, 1994; *Schott et al*., 1999]. Recently, *Våge et al*. [2011] showed very weak mean flows (±1 cm/s) over the western Reykjanes Ridge flank in the ISOW depth range based on repeated altimetric-referenced geostrophic velocity sections across the Irminger Basin during 1991–2007. Alternatively, some studies have shown evidence from water property distributions and high-resolution models that at least some ISOW spreads westward and/or northwestward from the CGFZ and do not loop through the Irminger Basin [*Stramma et al*., 2004; *Xu et al*., 2010]. Given the strong interaction between the NAC and ISOW in the CGFZ documented here, it is easy to imagine that the NAC could intermittently disrupt the smooth flow of ISOW along the isobaths northward from the CGFZ. How ISOW entering the western basin from the CGFZ is partitioned along these pathways is a topic of ongoing research.

Finally, in most of this paper, we have implied that the ISOW flow is passively "pushed around" by the NAC. In fact, there may be a dynamical connection between the two currents whereby the ISOW has some

influence on the path of the NAC. *Spall* [1996a,1996b] showed that the presence of the DWBC flowing southward along the U.S. East Coast alters the intermediate-depth potential vorticity distribution, which in turn affects the path of the separating Gulf Stream. Similarly, the presence of ISOW in the CGFZ may have some influence on where the NAC can cross the MAR. To address this possibility, a three-dimensional observational array, and a high-resolution regional numerical model would be needed to investigate the along-channel propagation of both NAC and ISOW transport anomalies. While the B1012 array has provided a more accurate estimate of ISOW transport through CGFZ than was possible previously, and allowed us to definitively connect the NAC to ISOW transport variability, the results have also put the spotlight on these and other fundamental unanswered questions about the deep circulation of the subpolar North Atlantic.

**Acknowledgments**

The authors are grateful for the substantial support for this project provided by M. Rhein of the University of Bremen, who secured ship time on German research vessels for both the deployment and recovery of the CGFZ mooring array. The captains, crews, and scientific parties on the *Meteor* and *Merian* warmly welcomed WHOI mooring technicians and provided excellent support for the CGFZ mooring operations. The authors also thank WHOI mooring technician B. Hogue for expertly leading both the deployment and recovery efforts. H.F. thanks A. Ramsey, F. Straneo, L. Trafford, and J. Toole for advice on mooring data processing, and A.B. thanks J. Toole for several helpful discussions regarding the analysis and interpretation of the mooring observations. The authors also acknowledge the thoughtful comments of two anonymous reviewers which helped to improve the manuscript. The altimeter products used here were produced by Ssalto/Duacs and distributed by Aviso, with support from CNES (http:///www.aviso.altimettry.fr/duacs/). The data presented in this paper are available from NCEI (http://accession.nodc.noaa.gov/0164585). This research was funded by the U.S. National Science Foundation through grant OCE-0926656 and by the Woods Hole Oceanographic Institution through the Henry Bryant Bigelow Chair for Excellence in Oceanography awarded to A.B. in 2014.

## References

Belkin, I. M., and S. L. Levitus (1996), Temporal variability of the Subarctic Front near the Charlie-Gibbs Fracture Zone, *J. Geophys. Res.*, *101*(C12), 28,317–28,324, doi:10.1029/96JC02794.

Bower, A. S., and W.-J. von Appen (2008), Interannual variability in the pathways of the North Atlantic Current over the Mid-Atlantic Ridge and the impact of topography, *J. Phys. Oceanogr.*, *38*(1), 104–120, doi:10.1175/2007JPO3686.1.

Bower, A. S., B. Le Cann, T. Rossby, W. Zenk, J. Gould, K. Speer, P. L. Richardson, M. D. Prater, and H.-M. Zhang (2002), Directly measured mid-depth circulation in the northeastern North Atlantic Ocean, *Nature*, *419*, 603–607, doi:10.1038/nature01078.

Bower, A. S., H. H. Furey, and L. Trafford (2017), *Water Temperature, Conductivity, and Others Collected From MOORINGS in North Atlantic Ocean From 2010–08-18 to 2012–06-30 (NCEI Accession 0164585)*, NOAA Natl. Cent. for Environ. Inf, Silver Springs, Md.

Daniault, N., et al. (2016), The northern North Atlantic Ocean mean circulation in the early 21st century, *Prog. Oceanogr.*, *146*, 142–158, doi:10.1016/i.pocean.2016.06.007.

Dickson, R. R., and J. Brown (1994), The production of North Atlantic Deep Water: Sources, rates, and pathways, *J. Geophys. Res.*, *99*(C6), 12,319–12,341, doi:10.1029/94JC00530.

Fer, I., G. Voet, K. S. Seim, B. Rudels, and K. Latarius (2010), Intense mixing of the Faroe Bank Channel overflow, *Geophys. Res. Lett.*, *37*, L02604, doi:10.1029/2009GL041924.

Fleischmann, U., H. Hildebrandt, A. Putzka, and R. Bayer (2001), Transport of newly ventilated deep water from the Iceland Basin to the Westeuropean Basin, *Deep Sea Res., Part I*, *48*(8), 1793–1819, doi:10.1016/S0967-0637(00)00107-2.

Furey, H. H., L. Trafford, and A. S. Bower (2014), A crossroads of the Atlantic Meridional Overturning Circulation: The Charlie-Gibbs Fracture Zone data report, August 2010-June 2012, *WHOI Tech. Rep. WHOI-2014–04*, 135 pp Woods Hole Oceanographic Institution, Woods Hole, Mass.

Harvey, J. G., and A. Theodorou (1986), The circulation of Norwegian Sea overflow water in the eastern North Atlantic, *Oceanol. Acta*, *9*(4), 393–402.

Kanzow, T., and W. Zenk (2014), Structure and transport of the Iceland Scotland Overflow plume along the Reykjanes Ridge in the Iceland Basin, *Deep Sea Res., Part I*, *86*, 82–93, doi:10.1016/j.dsr.2013.11.003.

Kieke, D., et al. (2014), Overflow, circulation & biodiversity - cruise no. MSM21/2 - June 25 - July-24, 2012 - Reykjavik (Iceland) - Nuuk (Greenland), in *MARIA S. MERIAN-Berichte, MSM21/2*, 5 pp., DFG-Senatskomm. für Ozeanogr., Bremen, doi:10.2312/cr_msm21_2.

Lankhorst, M., and W. Zenk (2006), Lagrangian observations of the middepth and deep velocity fields of the Northeastern Atlantic Ocean, *J. Phys. Oceanogr.*, *36*(1), 43–63, doi:10.1175/JPO2869.1.

Lozier, M. S., et al. (2017), Overturning in the Subpolar North Atlantic Program: A new international ocean observing system, *Bull. Am. Meteorol. Soc.*, *98*, 737–752, doi:10.1175/BAMS-D-16-0057.1.

Mauritzen, C., J. Price, T. Sanford, and D. Torres (2005), Circulation and mixing in the Faroese Channels, *Deep Sea Res., Part I*, *52*(6), 883–913, doi:10.1016/j.dsr.2004.11.018.

McCartney, M. S. (1992), Recirculating components to the deep boundary current of the Northern North Atlantic, *Prog. Oceanogr.*, *29*, 283−383, doi:10.1016/0079-6611(92)90006-L.

Meincke, J., and A. Sy (1983), Large scale effects of the Mid-Atlantic Ridge on the North Atlantic Current, ICES Hydrography Committee, CM, 100, 8–10.

Meinen, C. S., M. O. Baringer, and R. F. Garcia (2010), Florida Current transport variability: An analysis of annual and longer-period signals, *Deep Sea Res., Part I*, *57*(7), 835–846, doi:10.1016/j.dsr.2010.04.001.

Mercier, H., P. Lherminier, A. Sarafanov, F. Gaillard, N. Daniault, D. Desbruyeres, A. Falina, B. Ferron, T. Huck, and V. Thierry (2015), Variability of the Meridional Overturning Circulation at the Greenland-Portugal Ovide section from 1993 to 2010, *Prog. Oceanogr.*, *132*, 250–261, doi:10.1016/j.pocean.2013.11.001.

Østerhus, S., T. Sherwin, D. Quadfasel, and B. Hansen (2008), The overflow transport east of Iceland, in *Arctic-Subarctic Ocean Fluxes: Defining the Role of the Northern Seas in Climate*, edited by R. R. Dickson, J. Meincke, and P. Rhines, pp. 427–441, Springer, Dordrecht.

Rhein, M. (2010), *Cruise Report, RV Meteor: Cruise M82/2, from St. John's, Canada, to Ponta Delgada, Acores, Portugal, August 4th to September 1st, 2010*, 38 pp., Inst. für Umweltphys., AG Ozeanogr., Univ. Bremen, Bremen.

Rhein, M., J. Fischer, W. M. Smethie, D. Smythe-Wright, R. F. Weiss, C. Mertens, D.-H. Min, U. Fleischmann, and A. Putzka (2002), Labrador Sea water: Pathway, CFC inventory, and formation rates, *J. Phys. Oceanogr.*, *32*(2), 648–665, doi:10.1175/1520-0485(2002)032<0648:LSWPCI>2.0.CO;2.

Rhein, M., D. Kieke, S. Hüttl-Kabus, A. Roessler, C. Mertens, R. Meissner, B. Klein, C. W. Böning, and I. Yashayaev (2011), Deep water formation, the subpolar gyre, and the Meridional Overturning Circulation in the subpolar North Atlantic, *Deep Sea Res., Part II*, *58*(17–18), 1819–1832, doi:10.1016/j.dsr2.2010.10.061.

Roessler, A., M. Rhein, D. Kieke, and C. Mertens (2015), Long-term observations of North Atlantic Current transport at the gateway between western and eastern Atlantic, *J. Geophys. Res. Oceans*, *120*, 4003–4027, doi:10.1002/2014JC010662.

Rossby, T., C. Flagg, and K. Donohue (2010), On the variability of Gulf Stream transport from seasonal to decadal timescales, *J. Mar. Res.*, *68*(3–4), 503–522, doi:10.1357/002224010794657128.

Sarafanov, A., A. Sokov, A. Demidov, and A. Falina (2007), Warming and salinification of intermediate and deep waters in the Irminger Sea and Iceland Basin in 1997–2006. *Geophys. Res. Lett.*, *34*, L23609, doi:10.1029/2007GL031074.

Sarafanov, A., A. Falina, H. Mercier, P. Lherminier, and A. Sokov (2009), Recent changes in the Greenland-Scotland overflow-derived water transport inferred from hydrographic observations in the southern Irminger Sea, *Geophys. Res. Lett.*, *36*, L13606, doi:10.1029/2009GL038385.

Saunders, P. M. (1994), The flux of overflow water through the Charlie-Gibbs Fracture Zone, *J. Geophys. Res.*, *99*(C6), 12,343–12,355, doi:10.1029/94JC00527.
Schmitz, W. J., and N. G. Hogg (1978), Observations of energetic low-frequency current fluctuations in Charlie-Gibbs Fracture Zone, *J. Mar. Res.*, *36*(4), 725–734.
Schmitz, W. J., and M. S. McCartney (1993), On the North Atlantic circulation, *Rev. Geophys.*, *31*(1), 29−49, doi:10.1029/92RG02583.
Schott, F., L. Stramma, and J. Fischer (1999), Interaction of the North Atlantic Current with deep Charlie Gibbs Fracture Zone throughflow, *Geophys. Res. Lett.*, *26*(3), 369–372, doi:10.1029/1998GL900223.
Send, U., M. Lankhorst, and T. Kanzow (2011), Observation of decadal change in the Atlantic Meridional Overturning Circulation using 10 years of continuous transport data, *Geophys. Res. Lett.*, *38*, L24606, doi:10.1029/2011GL049801.
Smeed, D. A., et al. (2014), Observed decline of the Atlantic Meridional Overturning Circulation 2004–2012, *Ocean Sci.*, *10*(1), 29–38, doi:10.5194/os-10-29-2014.
Smethie, W. M., R. A. Fine, A. Putzka, and E. P. Jones (2000), Tracing the flow of North Atlantic Deep Water using chlorofluorocarbons, *J. Geophys. Res.*, *105*(C6), 14,297–14,323, doi:10.1029/1999JC900274.
Spall, M. A. (1996a), Dynamics of the Gulf Stream/Deep Western Boundary Current Crossover. Part I: Entrainment and recirculation, *J. Phys. Oceanogr.*, *26*(10), 2152−2168, doi:10.1175/1520-0485(1996)026<2152:DOTGSW>2.0.CO;2.
Spall, M. A. (1996b), Dynamics of the Gulf Stream/Deep Western Boundary Current crossover. Part II: Low-frequency internal oscillations, *J. Phys. Oceanogr.*, *26*, 2169−2182, doi:10.1175/1520-0485(1996)026<2169:DOTGSW>2.0.CO;2.
Srokosz, M. A., and H. L. Bryden (2015), Observing the Atlantic Meridional Overturning Circulation yields a decade of inevitable surprises, *Science*, *348*(6241), 1255575, doi:10.1126/science.1255575.
Stramma, L., D. K. Kieke, M. Rhein, F. Schott, I. Yashayaev, and K. P. Koltermann (2004), Deep water changes at the western boundary of the subpolar North Atlantic during 1996 to 2001, *Deep Sea Res., Part I*, *51*(8), 1033–1056, doi:10.1016/j.dsr.2004.04.001.
Sy, A. (1988), Investigation of large-scale circulation patterns in the central North Atlantic: The North Atlantic Current, the Azores current, and the Mediterranean Water plume in the area of the Mid-Atlantic Ridge, *Deep Sea Res., Part A*, *35*(3), 383–413, doi:10.1016/0198-0149(88)90017-9.
Sy, A., U. Schauer, and J. Meincke (1992), The North Atlantic Current and its associated hydrographic structure above and eastwards of the Mid-Atlantic Ridge, *Deep Sea Res., Part A*, *39*(5), 825–853, doi:10.1016/0198-0149(92)90124-C.
Toole, J. M., R. G. Curry, T. M. Joyce, M. McCartney, and B. Peña-Molino (2011), Transport of the North Atlantic Deep Western Boundary Current about 39°N, 70°W: 2004–2008, *Deep Sea Res., Part II*, *58*, 1768–1780, doi:10.1016/j.dsr2.2010.10.058.
Trenberth, K. E., and J. M. Caron (2001), Estimates of meridional atmosphere and ocean heat transports, *J. Clim.*, *14*, 3433–3443, doi:10.1175/1520-0442(2001)014<3433:EOMAAO>2.0.CO;2.
Våge, K., R. S. Pickart, A. Sarafanov, Ø. Knutsen, H. Ercier, P. Lherminier, H. M. van Aken, J. Meincke, D. Quadfasel, and S. Bacon (2011), The Irminger Gyre: Circulation, convection, and interannual variability, *Deep Sea Res. Part I*, *58*(5), 590–614, doi:10.1016/j.dsr.2011.03.001.
van Aken, H. M. (2000), The hydrography of the mid-latitude northeast Atlantic Ocean: I: The deep water masses, *Deep Sea Res., Part I*, *47*(5), 757–788.
Willis, J. K. (2010), Can in situ floats and satellite altimeters detect long-term changes in Atlantic Ocean overturning?, *Geophys. Res. Lett.*, *37*, L06602, doi:10.1029/2010GL042372.
Worthington, L. V., and G. H. Volkmann (1965), The volume transport of the Norwegian Sea overflow water in the North Atlantic, *Deep Sea Res. Oceanogr. Abstr.*, *12*, 667–676, doi:10.1016/0011-7471(65)91865-6.
Xu, X., W. J. Schmitz Jr., H. E. Hurlburt, P. J. Hogan, and E. P. Chassignet (2010), Transport of Nordic Seas overflow water into and within the Irminger Sea: An eddy-resolving simulation and observations, *J. Geophys. Res.*, *115*, C12048, doi:10.1029/2010JC006351.
Yashayaev, I., and B. Dickson (2008), Transformation and fate of overflows in the Northern North Atlantic, in *Arctic-Subarctic Ocean Fluxes: Defining the Role of the Northern Seas in Climate*, edited by R. R. Dickson, J. Meincke, and P. Rhines, pp. 505–526, Springer, Dordrecht.